Doubly magic ^{208}Pb: High-spin states, isomers, and E3 collectivity in the yrast decay

R. Broda, R. V. F. Janssens, Ł. W. Iskra, J. Wrzesinski, B. Fornal, M. P. Carpenter, C. J. Chiara, N. Cieplicka-Oryńczak, C. R. Hoffman, F. G. Kondev, W. Królas, T. Lauritsen, Zs. Podolyak, D. Seweryniak, C. M. Shand, B. Szpak, W. B. Walters, S. Zhu, and B. A. Brown

Phys. Rev. C **95**, 064308 — Published 12 June 2017

DOI: 10.1103/PhysRevC.95.064308

Doubly-magic ^{208}Pb: High-spin states, isomers and *E*3 collectivity in the yrast decay

R. Broda,[1] R. V. F. Janssens,[2] Ł. W. Iskra,[1] J. Wrzesinski,[1] B. Fornal,[1] M. P. Carpenter,[2] C. J. Chiara, [2,3,*] N. Cieplicka-Oryńczak,[1] C. R. Hoffman,[2] F. G. Kondev,[4] W. Królas,[1] T. Lauritsen,[2] Zs. Podolyak,[5] D. Seweryniak,[2] C. M. Shand,[5] B. Szpak,[1] W. B. Walters,[3] S. Zhu,[2] and B.A. Brown,[6]

[1]Institute of Nuclear Physics, Polish Academy of Sciences, PL-31-342 Kraków, Poland

[2]Physics Division, Argonne National Laboratory, Argonne, Illinois 60439, USA

[3]Department of Chemistry and Biochemistry, University of Maryland, College Park. Maryland 20742, USA

[4]Nuclear Engineering Division, Argonne National Laboratory, Argonne, Illinois 60439, USA

[5]Department of Physics, University of Surrey, Guildford, GU2 7XH, United Kingdom

[6]Department of Physics and Astronomy and National Superconducting Cyclotron Laboratory, Michigan State University, East Lansing, Michigan 48824-1321, USA

PACS numbers: 23.20.Lv, 21.60.Cs, 27.80.+w, 23.35.+g, 23.20.En

Abstract:

Yrast and near-yrast levels up to spin values in excess of $I = 30\hbar$ have been delineated in the doubly-magic ^{208}Pb nucleus following deep-inelastic reactions involving ^{208}Pb targets and, mostly, 430-MeV ^{48}Ca and 1440-MeV ^{208}Pb beams. The level scheme was established up to an excitation energy of 16.4 MeV, based on multi-fold γ-ray coincidence relationships measured with the Gammasphere array. Below the well-known, 0.5-μs 10^+ isomer, ten new transitions were added to earlier work. The delineation of the higher parts of the level sequence benefited from analyses involving a number of prompt- and delayed-coincidence conditions. Three new isomeric states were established along the yrast line with $I^\pi = 20^-$ (10342 keV), 23^+ (11361 keV), and 28^- (13675 keV), and respective half-lives of 22(3), 12.7(2), and 60(6) ns. Gamma transitions were also identified preceding in time the 28^- isomer, however, only a few could be placed in the level scheme and no firm spin-parity quantum numbers could be proposed. In contrast, for most states below this 28^- isomer, firm spin-parity values were assigned, based on total electron-conversion coefficients, deduced for low-energy (<500 keV) transitions from γ-intensity balances, and on measured γ-ray angular distributions. The latter also enabled the quantitative determination of mixing ratios. The transition probabilities extracted for all isomeric transitions in ^{208}Pb have been reviewed and discussed in terms of the intrinsic structure of the initial and final levels involved. Particular emphasis was placed on the many observed *E*3 transitions as they often exhibit significant enhancements in strength (of the order of tens of W.u.) comparable to the one seen for the neutron $j_{15/2} \rightarrow g_{9/2}$ *E*3 transition in ^{209}Pb. In this context, the enhancement of the 725-keV *E*3 transition (56 W.u.) associated with the decay of the highest-lying 28^- isomer observed in this work remains particularly challenging to explain. Large-scale shell-model calculations were performed with two approaches, a first one where the 1, 2, and 3 particle-hole excitations do not mix with one another, and another more complex one, in which such mixing takes place. The calculated levels were compared with the data and a general agreement is observed for most of the ^{208}Pb level scheme. At the highest spins and energies, however, the

correspondence between theory and experiment is less satisfactory and the experimental yrast line appears to be more regular than the calculated one. This regularity is notable when the level energies are plotted versus the $I(I+1)$ product and the observed, nearly linear, behavior was considered within a simple "rotational" interpretation. Within this approximate picture, the extracted moment of inertia suggests that only the 76 valence nucleons participate in the "rotation" and that the ^{132}Sn spherical core remains inert.

---

*: Present address: U.S. Army Research Laboratory, Adelphi, Maryland 20783, USA

1. Introduction

The region of nuclei around "doubly-magic" ^{208}Pb has for many years been the subject of much experimental and theoretical research as it is viewed as one of the best locations on the periodic chart to evaluate shell-model descriptions of nuclear systems. At present, the understanding of the intrinsic structure of many excitations observed in nuclei neighboring ^{208}Pb is rather detailed. By now, the single-particle states of the major shells below and above the proton Z = 82 and neutron N = 126 magic numbers have been determined based on experiment. Residual interactions between nucleons occupying these orbitals, derived already in 1970 by Kuo and Herling [1], and subsequently readjusted taking into account new experimental results, have proved quite successful in reproducing the observed levels as shown, for instance, by Warburton and Brown [2]. Furthermore, theoretical efforts to determine residual interactions directly from the Bonn potential for free nucleons proved to be successful as well: this was demonstrated, for example, in the case of the two-proton nucleus ^{210}Po by Corragio *et al*. [3], and by other shell-model calculations particularly those describing excitations associated with neutron holes in the ^{208}Pb core (see [3] and refs. therein).

Possibilities to test the shell model further and to readjust and improve some of the residual interactions have expanded since the early 1990s stimulated by the use of large gamma-ray detector arrays which enabled spectroscopic investigations of high-spin states populated in deep-inelastic, heavy-ion induced reactions [4] that could not be explored earlier. In the ^{208}Pb region, this development resulted in the delineation of excitations associated with rather pure configurations, including many isomers arising from the energy-favored coupling of the available valence particles and holes. High-spin levels up to nearly I = 30 spin values were established in many nuclei often quite distant from the closed ^{208}Pb core, such as ^{203}Hg [5], ^{204}Hg [6], ^{204}Tl [7], ^{205}Tl [8], and ^{206}Bi [9]. Somewhat lower-spin yrast structures were studied in the closer neighbors; *e.g*., ^{207}Pb [10], ^{209}Pb [11], ^{207}Tl [12], and ^{206}Hg [13]. It is worth pointing to the recent review of metastable states of Ref. [14] as it includes many of the isomers of interest in the Pb region.

Whereas the structure of yrast levels arising from excitations within the available space of valence particles and holes could be understood within the shell model, as the calculated level energies matched rather well with the experimental ones, the structure of higher-spin states involving core excitations was generally found to be less transparent in nuclei neighboring ^{208}Pb. Here, the most striking phenomenon has been the regular appearance of distinct yrast states resulting from the maximum spin coupling of the 3^- lowest ^{208}Pb excitation with the highest-spin multi-particle state available from the valence particles and holes. Their energies appear to follow the simple additivity of interactions [15] established earlier, based on observed levels in which the 3^- level is coupled to the individual particle and hole constituents that contribute to their more complex structure. The understanding of other higher-spin states, located above these yrast levels involving the 3^- core excitation, still requires further experimental information, especially regarding firm spin-parity assignments. However, a more detailed investigation of high-spin states in the ^{208}Pb core itself appears to be crucial as well.

In the history of experimental investigations of ^{208}Pb, a large number of nuclear reactions and a large variety of techniques have been used. The experimental data were reviewed and summarized in 2007 by Martin[16]. Essentially, up to an excitation energy of 4.6 MeV, all the levels predicted by the shell model have been observed and assigned. However, a more complete set of 148 states has been listed and discussed in the study of Ref. [17] following (d, pγ) and (t, αγ) reactions. The latter work extends to a 7.4 MeV excitation energy and covers a spin range from the ground state up to the highest-spin 14^- level at 6744 keV. This 14^- state corresponds to the excitation with the highest spin achievable with a one-particle one-hole (1p-1h) configuration. It was originally identified along with several other high-spin levels in the (e, e') study by Connelly *et al*. [18] which determined the level energies with a few keV accuracy. The first observation of γ decays from these levels was reported by Schramm et al. [19] in an experiment using deep-inelastic, heavy-ion reactions that provided more precise level energies and initiated efforts to investigate ^{208}Pb in a higher-spin range. Preliminary results, reported in Refs. [10,20], established a few higher-spin states and indicated the presence of a 28-ns isomer. A more complete scheme of levels located above the 10^+ isomer in ^{208}Pb was presented in Refs. [4,21,22]. It was noted that the data did not allow then to clarify the location of higher-lying isomers, nor did they provide the information necessary for firm spin-parity assignments. As will be demonstrated below, these difficulties could be fully resolved in the present study where the most complete study of the ^{208}Pb high-spin levels available thus far is presented. From spectroscopy following deep-inelastic heavy-ion reactions, the ^{208}Pb level scheme is delineated up to the 13.7-MeV, $I^\pi = 28^-$ isomer. Above this long-lived state, a few higher-spin levels, up to an excitation energy of 16.4 MeV are presented as well.

On the theoretical side, the most complete shell-model calculations of ^{208}Pb excited states were performed by Brown [23]. These include all of the orbitals in the four major shells near the Fermi surface while considering a full two-particle two-hole (2p-2h) basis. Although Ref. [23] was mainly focused on properties of double-octupole excitations, the results concerning high-spin levels, of both negative and positive parity, were presented for a spin range up to $I = 18$. Satisfactory agreement was achieved with the experimental energies of levels known at that time; *i.e.,* up to the 14^- level. In the present work, more detailed results of these calculations will be confronted with the newly established experimental level scheme. In the most recent publication on ^{208}Pb [24], an extensive study of the (p, p'), (d, p), and (d, d') reactions was presented with the claim of complete identification of states below 6.2 MeV. The main part of the present work addresses ^{208}Pb states with higher spins and excitation energies.

2. Experimental procedures and data analysis

In a series of γ-ray spectroscopy experiments, performed at Argonne National Laboratory, the ^{208}Pb nucleus was produced in a number of heavy-ion induced collisions with yields enabling studies of its level structure up into a novel range of high angular momenta and excitation energies. Two of these measurements, in which 50- and 75-mg/cm^2 thick, 99% enriched ^{208}Pb targets were bombarded with 330-MeV ^{48}Ca and 1440-MeV ^{208}Pb beams, provided coincidence data with the highest statistics and/or the best peak-to-background ratio. As a result, they were mostly used in the present study. Nevertheless, available data from other experiments with ^{76}Ge and ^{82}Se beams bombarding the ^{208}Pb targets as well as with ^{48}Ca and ^{208}Pb beams on ^{238}U targets, all at energies 15 - 25% above the respective Coulomb barriers,

were often also inspected in the course of the analysis as cross-checks for some of the observations. All the heavy-ion beams were provided by the ATLAS superconducting linear accelerator and, in every case, a pulsing with a 412-ns repetition rate and an intrinsic pulse width of about 0.3 ns was used. Gamma rays were collected in a standard coincidence mode with the Gammasphere array [25]. This spectrometer consists of 101 Compton-suppressed, high-purity germanium detectors. The trigger enabled the recording of all multi-fold coincidence events, including also the two-fold ones. For specific cases, these lower-fold events turned out to be essential in order to achieve suitable statistical accuracy without giving up selectivity for the γ–ray sequences of interest. This was particularly important in the angular-distribution analysis and, in general, involved the most intense transitions.

The main part of the analysis employed the three- and higher-fold coincidence events which were sorted into cubes with various timing conditions. In the following, the letter P is used to indicate prompt γ transitions registered in the 0 - 30 ns time range with respect to the beam pulse, while the letter D denotes delayed transitions occurring between the beam bursts in an ad-hoc selected range that could extend up to 800 ns. Whereas a general overview of the ^{208}Pb level scheme was provided by the analysis of straightforward PPP and DDD coincidence cubes; *e.g.*, establishing the general population pattern of levels and revealing the presence of new isomers and γ-ray cascades, the detailed study of different parts of the level scheme required specific selections of events with more complex and optimized timing conditions. In particular, the presence of the well-known 10^+, $T_{1/2}$ = 0.5 μs isomer [26] provided a suitable selection criterion for events involving transitions located above this long-lived state. The latter transitions were the main object of the present study. Thus, PPD, PDD, PdD and ddD cubes were constructed, where the small letter d denotes delayed γ rays occurring within time ranges shorter than the full D range. Such data were used to obtain selectively from the coincidence cubes the required coincidence matrices by placing gates on the D axis for the most intense transitions associated with the decay of the 10^+ isomer. More specific details of this coincidence analysis will be discussed below in conjunction with the presentation of the ^{208}Pb level scheme and the determination of new isomeric half-lives. A particular emphasis was also placed in this work on spin-parity assignments, and a separate section is devoted to the associated analysis. These I^π assignments involve the extraction of total conversion coefficients for a number of low-energy transitions as well as the analysis of angular distributions which, in many instances, provided important, unambiguous results.

It has to be emphasized that the availability of the two main data sets discussed above proved essential to obtain reliable results. Indeed, while the statistics obtained in the ^{208}Pb + ^{208}Pb experiment was higher by about a factor 3, the complexity of the spectra was often challenging as they involved transitions from the highly-excited and broadly distributed complementary reaction fragments. On the other hand, the lower statistics data from the ^{48}Ca + ^{208}Pb reaction turned out to be much cleaner as the number of complementary Ca isotopes was smaller and the resulting spectra less complex. Surprisingly, the population of high-spin states in ^{208}Pb was found to be rather similar for both colliding systems, with a slight but distinct advantage for the ^{48}Ca + ^{208}Pb data.

3. Experimental results

A. Level scheme construction and isomeric states

In view of the statistical significance of the available data sets, it seemed worthwhile to start the analysis by revisiting the well-studied, lower part of the ^{208}Pb level scheme that involves yrast and near-yrast levels up to the region of the 10^+ isomer at 4895 keV [26]. The DDD coincidence data provided clear evidence for seven new transitions connecting states established previously in the decay of the 10^+ isomer. The coincidence spectra displayed in Fig.1 document the existence of four of these newly-placed γ rays associated with the deexcitation of the 3.2-ns, 8^+ level at 4611 keV [26]. The new transitions represent weak decay branches parallel to the two stronger ones established earlier. The double gates indicated in the four panels of Fig. 1 were placed in the DDD cube on the two strongest transitions depopulating each of the levels fed directly by the new γ rays and their placement is confirmed by their observation in the respective coincidence spectra. As discussed below, intensity balance considerations enabled the extraction of the total electron conversion coefficients, herewith establishing the *M2* character of the 404- and 228-keV transitions (Figs. 1(a) and 1(c)), and the *E*2 multipolarity of the 187-keV line (Fig. 1(b)). These observations confirm earlier spin-parity assignments for the levels involved. It then follows that the 902-keV γ ray in Fig. 1(d) has to be defined as a new *E*3-decay branch from the 4611-keV, 8^+ level. All of these new transitions have intensities smaller than 1% of the 10^+ isomeric decay intensity, with the weakest one at 228 keV (less than 0.1%) being close to the detection limit. These newly identified decay paths add to the systematics of transition rates in the ^{208}Pb nucleus.

The part of the ^{208}Pb level scheme discussed above is presented in Fig. 2. It includes predominantly the medium-spin, yrast and near-yrast levels populated in the 10^+ isomer decay. The arrow widths in Fig. 2 reflect the prompt population of the levels. Note that some of the known [16], less intense transitions have been omitted in Fig. 2 as the emphasis is placed on the newly observed ones, indicated in red color. The latter also include the three new prompt γ rays that bypass the 10^+ isomer; these were identified in the analysis of the prompt PPP coincidence cubes. One of these (150 keV) depopulates the previously established 9^+ level at 5011 keV through a path parallel to the one involving the strong 400-keV transition. Two γ rays with energies of 466 and 716 keV establish a new level at 5326 keV which very likely is the third 9^+ state, just above the second known 9^+ one at 5162 keV, also present in the data.

The information relevant for this part of the ^{208}Pb level scheme is listed in Table I. The prompt transition intensities quoted in the table reflect the integrated population from all deep-inelastic reaction channels in the ^{208}Pb + ^{208}Pb system leading to the states of interest. Several channels are often involved as complementary fragments associated with evaporation of a differing number of neutrons are observed. The reader is referred to the caption of Table I for further relevant information.

The main part of the present study was focused on the high-spin ($I \geq 10$) states located above the 0.5-μs, 10^+ (4895-keV) isomer. It turned out that all these levels ultimately ended up populating this 10^+ isomer and that no decay path was observed that bypasses it toward any other level of Fig. 2. This finding simplified the analysis since the requirement of observing coincidence relationships with well-known delayed transitions in the isomer decay provided a

clear means of identification of all transitions located above the long-lived state as well as a means to inspect their mutual coincidence relationships in a selective way. This is illustrated by the coincidence spectra of Fig. 3 obtained from the ^{208}Pb + ^{208}Pb experiment. These spectra include essentially all the transitions identified above the 10^+ isomer and reflect in separate panels the prompt and delayed population intensities. Figures 3(a) and 3(c) present the low- and high-energy parts of the prompt (P) spectrum selected from the PDD cube by placing double delayed gates on transitions below the 10^+ isomer. In Figs. 3(b) and 3(d), the corresponding spectra originate from the ddD cube with double gates on all combinations involving, on the one hand, strong delayed (D) transitions below the 10^+ isomer and on the other the most intense higher-lying transitions exhibiting a delayed (d) component in the 30- to 120-ns time range. As discussed below, three higher-lying isomers could be identified in ^{208}Pb and the intensities of the γ rays observed in Figs. 3(b) and 3(d) represent the integrated population of all of these. The main ^{208}Pb transitions are labelled by their energy in Fig. 3; many weaker ones remain unmarked for clarity. The complexity of the prompt spectra of Figs. 3(a) and 3(c) is increased further by the presence of lines from other Pb isotopes produced as complementary fragments by the reaction process. The strongest of these cross-coincident γ rays are identified by symbols defined in the legend of Fig. 3. It has to be kept in mind that the final identification of the ^{208}Pb transitions discussed hereafter also relied on a similar analysis of the ^{48}Ca + ^{208}Pb data (see above).

The ^{208}Pb level scheme of Fig. 4 was delineated mostly by using prompt PP coincidence matrices extracted from the PPD cubes by placing delayed gates along the D axis on transitions belonging to the isomeric decay. Nevertheless, the complete analysis also took advantage of the study of delayed dd coincidence events selected from the ddD cube as well as of a number of PD matrices extracted from the PDD cubes under a number of time ranges for the delayed γ rays. These PD matrices enabled the unambiguous placement of the three new isomers identified in the present study. Note that, for clarity, the level scheme of Fig. 4 starts from the 10^+ isomer at 4895 keV, and also includes the states located above the highest-lying long-lived (60 ns) level, despite the fact that their placement is less certain, as discussed at the end of this section. The spin and parity assignments proposed in Fig. 4 are discussed separately in the next section. Table II provides the full list of states established in ^{208}Pb above the 10^+ isomer with the relevant information on level and transition energies, prompt and delayed intensities of depopulating transitions as well as γ-ray multipolarities and adopted spin-parity assignments.

In the strongly populated lowest part of the level scheme (Fig. 4) extending to the 6744-keV 14^- state, the present data confirmed all of the previously reported levels [21] and identified a new one at 6435 keV linked by 1200- and 686-keV transitions to the two lower-lying 11^+ states. This state most likely corresponds to the 12^-, 6437(6)-keV level first observed and assigned in the (e, e') experiment [18] and the γ decay reported here confirms the assignment. In addition, several transitions not observed in earlier works could now be placed between well-established levels: these include the relatively intense 1206- and 1379-keV lines as well as much weaker ones at 514, 643, 699, and 1213 keV (see Fig. 4 and Table II). Two examples of relevant spectra, obtained from the preselected PP matrix described above, are displayed in Figs. 5(a) and 5(b). In Fig. 5(a), the coincidence gate placed on the 680-keV transition between the 11^+, 5750-keV and 10^+, 5069-keV states demonstrates the quality of coincidence relationships observed for a relatively weak branch involved in the depopulation of high-spin levels. The 174- and 351-keV lines are seen prominently in the spectrum and represent the intensity of this branch as they, respectively, follow and precede the gating transition in the

sequence. The 686- and 699-keV lines, listed among the new, weaker transitions above, are clearly present as well, and could be placed as additional transitions feeding the 11^+ level, despite the fact that their intensities are close to the detection limit. In such cases, the presence of the weak lines was always confirmed through inspection of other coincidence data so that they could be placed with confidence in the level scheme of Fig. 4.

The main feeding of the 14^-, 6744-keV state is shared among several high-energy transitions and each of them could be clearly located with the observed coincidence relationships. The most intense one, which is also the highest-energy one at 2318 keV, was particularly useful in delineating the upper part of the level scheme since coincidence spectra involving it as a gate excluded the many complex level sequences populated in the parallel decays (Fig. 4). On the other hand, the part of the level scheme involving the latter branches was the most challenging to establish uniquely in the present analysis. Figure 5(b) was obtained as a sum of coincidence spectra with gates placed on the lines at 1231, 1284, and 1579 keV representing the dominant decay paths parallel to the 2318-keV transition. The 212-, 250-, 324-, and 786-keV transitions seen in this spectrum were unambiguously placed in the level scheme as shown in Fig. 4 on the basis of detailed analyses of this and additional coincidence data where these lines were involved as gates. The placements were aided by the presence of a number of other, much weaker, cross-over transitions (see Fig. 4 and Table II).

The strong 291-keV line consists of a doublet of transitions which are in mutual coincidence and are separated in energy by only 1.1 keV. It was possible to determine the energy and relative intensity of each component (Table II) as well as to establish the respective placements in the level scheme. Clearly, the higher-energy component at 291.3 keV is the most intense yrast transition depopulating the 9394-keV level, a state that collects almost all of the intensity from higher-lying levels. The lower-energy 290.2-keV transition, on the other hand, depopulates the 9103-keV level fed by the 291.3-keV γ ray and initiates the subsequent decay via all the branches parallel to the 2318-keV transition. The observed strong coincidence between the 2318- and 291.3-keV lines required the placement of a low-energy, 41.7-keV connecting transition. The latter was not observed, due in part to the poor timing response and strongly reduced detector efficiency in this low-energy region. In addition, the expected large electron conversion coefficient ($\alpha_{tot}(M1) = 22$) also excluded its direct observation. Thus, the quantitative results for this transition only include its energy and total transition intensity as inferred from the relevant coincidence spectra (see Table II). Similar difficulties were encountered with the observation of two other low-energy transitions: the 53.0-keV γ ray linking the 8027- and 7974-keV levels, and the lower intensity 89.3-keV line between the 8813- and 8724-keV states. Both transitions remained unobserved and their existence, energies, and total transition intensities, including electron conversion, were deduced from the coincidence spectra. It is worth mentioning that this 89.3-keV transition populates yet another decay branch parallel to 2318-keV γ ray that includes the 459- and 237-keV lines that can be seen in Fig. 5(b).

Above the 9394-keV level, four γ transitions are placed of which the strongest, of 948 keV, was established to be the main decay path from the 22-ns isomer located at 10342 keV. The spectra displayed in the 550 – 1700 keV energy range in Figs. 6(a) and 6(b) were obtained by placing gates on the 291-keV doublet in the PP and dd matrices, preselected by also requiring the presence of γ rays from the 10^+ isomeric decay. These data show the prompt (Fig. 6(a)) and delayed (Fig. 6(b)) transitions occurring above and below the 9394-keV state. It is worth noting that the cross-coincidence transitions assigned to complementary Pb isotopes,

identified in Fig. 6(a) and explained in the legend, involve lower-mass isotopes than observed in Figs. 3(a) and 3(c). This reflects the fact that, by requiring ^{208}Pb excitations with higher-spin and energy, one selects more violent deep-inelastic collisions that involve the evaporation of a larger number of neutrons.

A comparison of Figs. 6(a) and 6(b) indicates that, apart from the strong delayed 948-keV isomeric transition, the 742-, 802-, and 963-keV γ rays feeding the 9394-keV level are mostly the result of prompt feeding. Here, above the 742-keV transition, the 160-, 235-, and 395-keV lines establish the two higher-lying levels at 10371 and 10531 keV which have no connection to the extended level structure built on the 22-ns isomer, but the linking 175-keV transition connects these two states to the 10196-keV level depopulated by the 802-keV line. Whereas an additional, weak 357-keV transition was placed above the 10196-keV level and establishes the new 10552-keV state, no transitions could be observed to lie above the relatively strong prompt 963-keV γ ray. In the decay from the 10342-keV isomeric state, two additional weak decay branches that compete with the 948-keV transition could be established. One of these is the 146-keV line that feeds the 10196-keV state, herewith explaining the presence of a delayed component for the 802-keV line (Fig. 6(b)). The other weak branch consists of the 206- and 1033-keV transitions that depopulate the 22-ns isomer in a short cascade to the 9103-keV level. The ordering of the two γ rays was determined on the basis of the prompt intensities.

The upper part of the ^{208}Pb level scheme of Fig.4, above the 10342-keV isomer, exhibits a particularly simple structure and, with the help of the PD coincidence matrices discussed above, the placement of the transitions and the location of higher-lying isomeric states were achieved in a rather straightforward manner. Among the γ rays preceding in time the 948-keV transition, the 1019-keV line is the most intense and was determined to be the only one depopulating the 13-ns isomer at 11361 keV. Based on the coincidence relationships, the fairly intense 592-keV prompt γ ray was placed in parallel with the 1019-keV transition, herewith establishing the 10934-keV state with no connection to the 13-ns isomer or any higher-energy level. All of the other transitions in this part of the level scheme were found to be preceding in time both the 13-ns, 11361-keV and 22-ns, 10342-keV isomers and could be placed with confidence on the basis of the observed coincidence relationships and the measured prompt and delayed intensities (see Table II). The delayed dd coincidence spectra of Fig. 7 also provided strong confirmation of this part of the level scheme through the presence of yet another high-spin isomeric state located at an energy of 13675 keV with a measured 60-ns half-life. The gates placed on the most intense 1019-, 1588-, and 725-keV transitions in Figs. 7(a), 7(b), and 7(c) provide spectra representative of the quality of the delayed coincidence data used in the analysis. The prompt population of the 597-keV γ ray from the 11958-keV level fixed unambiguously its placement below the 991-keV feeding transition, and a similar argument established the ordering of the 139- and 587-keV lines in the decay of the highest long-lived state. The presence of the 139-keV isomeric decay branch is documented in Fig. 8(a) through a coincidence spectrum obtained with a gate on the 587-keV transition. Figures. 8(b) and 8(c) display the low-energy parts of coincidence spectra with gates on the 802- and 1033-keV transitions and provide evidence for two other transitions representing weak decay branches from the 22-ns, 10342-keV isomer. The spectrum of Fig. 8(b) is somewhat compromised by contributions from the 803-keV ^{206}Pb transition in the gate, but nevertheless shows the 146-keV line depopulating the isomer to the 10196-keV level, while Fig. 8(c) provides evidence for the 206-keV decay branch populating the 10136-keV state.

The isomeric state half-lives were determined from the time distributions between γ rays located above the specific isomer and those featuring prominently in the associated decay. The appropriate sorting of the G_1G_2T coincidence cubes, where G1 and G2 denote the prompt and delayed transition energies, respectively, and T is the time parameter, resulted in the time distributions displayed in Figs. 9(a) and 9(b). In panel (a), the decay curves for the three new isomers are presented. The gate placements appropriate for each long-lived state are indicated, and the half-lives resulting from the fits are given as well with their respective errors. It should be noted that previous work [21] had reported the presence of delayed high-spin transitions with a 28(8)-ns half-life in ^{208}Pb, a value that agrees within error with the present $T_{1/2}$ = 22(3) ns value for the 10342-keV isomer. However, the earlier determination did not take into account feeding from the two higher-lying long-lived states, while the present analysis does. The half-life of the 11361-keV isomer was determined to be 12.7(15) ns, and a 60(6) ns value was extracted for the highest-spin, long-lived state at 13675 keV. In the latter case (bottom of Fig. 9(a)), the G1 gate was placed on the 7 strongest prompt transitions placed above the isomer; the latter γ rays are discussed below. The decay curve displayed in Fig. 9(b) was instrumental in determining the half-life for the 10^+, 4895-keV isomer. The present value, $T_{1/2}$ = 0.57(5) μs, agrees well with the previous 0.50(5) μs one [26], and the average value of 0.535(35) μs is adopted for later considerations.

A dedicated analysis was also carried out to search for yet higher-spin levels; *e.g.*, states located above the 60-ns isomer at 13675 keV. As outlined above, the identification of such states was important as the transitions involved were used to extract the isomeric half-life. Furthermore, the exploration of the level structure in this high-energy regime provides an opportunity to reach a region involving three particle-hole excitations. The 60-ns half-life enabled an optimal selection of the ad-hoc PDD cube from which prompt coincidence spectra of transitions preceding in time γ rays emitted in the 30 - 110 ns time range could be extracted. The double DD gates were placed on all intense lines in the isomeric decay down to the 6744-keV, 14^- level. Additional gates on lower-lying transitions were avoided as they were found to add unwarranted complexity to the data. Sample results from this analysis for the ^{208}Pb + ^{208}Pb and ^{48}Ca + ^{208}Pb reactions are presented in Figs. 10(a) and 10(b), respectively. In both spectra, the ^{208}Pb transitions are marked by their energies and frames surround the new transitions deexciting states located above the 13675-keV isomer. The presence in Fig. 10(a) of many transitions from complementary fragments (lower-mass Pb isotopes, see discussion above) represented a significant challenge which was best addressed by the inspection of coincidence data from the other reaction. Thus, the spectrum of Fig. 10(b) demonstrates the practical importance of the ^{48}Ca + ^{208}Pb data set. While the statistical accuracy of this spectrum is lower by at least a factor of four, it is also less complex as it involves only a few transitions from complementary Ca isotopes. As such, it provided confirmation of the identification of 11 ^{208}Pb transitions above the 60-ns isomer. These new transitions are listed in Table III and the transition energies were averaged from both data sets. On the other hand, the intensities are listed separately for the two reactions, since some of the observed differences likely reflect differing population patterns, with the ^{48}Ca measurement favoring feeding at higher spin.

With the identification of the highest-lying transitions achieved as described above, the prompt (PP) coincidence matrix obtained with less selectivity by placing gates on single-delayed (D) transitions in the PPD cube was employed in the delineation of the upper part of the level scheme, above the 13675-keV isomer. In general, the transitions are rather weak and

close to the detection sensitivity of the present investigation. Nevertheless, from the observed coincidence relationships, a cascade of four transitions was established with respective energies of 341, 578, 862, and 907 keV. Their ordering is based on the measured intensities (Table III). On the other hand, the relatively strong 1208-keV γ ray did not show a coincidence with any other transition from Table III and was, thus, placed as depopulating the 14883-keV level directly to the isomer. One may note that a comparison of the intensities determined in both data sets (Table III) favors the non-yrast character reflected in the spin assignment of this state. In contrast, the intensities of the two highest γ rays in the four-transition cascade appear to be consistent with the higher spin values favored by the ^{48}Ca data. The rather intense 189-, 677-, and 723-keV transitions seen in Fig. 10 could not be placed. The 677-keV transition likely feeds the 14016-keV level, but the relation of this line with the mutually coincident 189-, 723-keV transitions could not be resolved with the available statistics. This may well indicate that all three transitions are part of a more complex level structure that will only be elucidated with additional data.

B. Electron-conversion coefficients, γ-ray angular distributions, and spin-parity assignments

In the present work, the spin-parity values assigned to the levels observed in ^{208}Pb are in most instances based on α_{tot} electron-conversion coefficients (ECC) extracted from intensity-balance arguments and on measured γ-ray angular distributions. For the low-energy lines listed in Table IV, appropriate gating conditions in the coincidence histograms provided data suitable to obtain the transition yields required to extract α_{tot} ECC, based on intensity balance considerations. Useful results could be obtained up to energies of about 400 keV, herewith enabling a unique determination of the multipolarity of most transitions listed in Table IV. The latter include the 187-, 228-, and 404-keV transitions located in the lower part of the ^{208}Pb level scheme (see Fig. 2) as well as the 174-, 295-, 340-, 348-, and 351-keV ones from the strongly populated levels below the 14^- state. Although all of these transitions depopulate levels for which spin-parity assignments had been proposed earlier, the present results should be viewed as completing the available experimental information and confirming these assignments. On the other hand, the ECC results listed in Table IV for transitions from the higher part of the level scheme proved vital for spin-parity assignments, as discussed below. It should be noted that, in this analysis, the 290.2- and 291.3-keV doublet could be resolved, herewith providing crucial characterization of both as *E*1 and *M*1 dipole transitions, respectively. In the case of the rather weak 138.7- and 145.8-keV lines, the multi-gated delayed coincidence spectrum of Fig. 3(b) had to be used to extract the α_{tot} ECC values by requiring an intensity balance with the 587- and 802-keV transitions, respectively.

Analysis of the γ-ray angular distributions provided particularly useful results as they reflect the surprisingly large spin alignment of the reaction products in the ^{208}Pb + ^{208}Pb system. Two-fold data were of sufficient statistics in spectra obtained with coincidence gates appropriately selected to enable the optimal extraction at each angle of the intensity of γ rays of interest. Spectra from calibration sources were used to normalize the yields measured from the 11 rings of detectors located at different angles θ with respect to the beam direction. In the final analysis, the data were reduced to six angles (17, 35, 53, 70, 80, and 90 deg.) by adding spectra from forward and backward rings located symmetrically around 90 deg. Samples of the measured distributions are displayed in Fig. 11 and a complete list of all the results can be found in Table V. The data were usually fit with the conventional expansion in terms of Legendre polynomials; *i.e.,* $W(\theta) = A_0(1 + A_2/A_0P_2(\cos\theta) + A_4/A_0P_4(\cos\theta))$.

However, in instances where statistics proved insufficient, the A_4 term was neglected as can be seen in Table V. Some examples of Fig. 11 were selected to display the angular distributions measured for important $E3$ transitions (725, 1019, 1508, and 2318 keV). These are characterized by large, positive A_2 values that can be contrasted with the even larger, but negative A_2 coefficients obtained for the uniquely assigned $\Delta I = 1$, $M1/E2$ mixed 295- and 1284-keV transitions. Two transitions (291- and 865-keV) are also included in Fig. 11 as examples of nearly isotropic distributions, apparently pointing to specific $M1/E2$ mixing ratios.

Columns 7 and 8 of Table V list the adopted multipolarity and the $\delta(M1/E2)$ mixing ratio extracted from the measured distribution coefficients for each transition. The latter ratios required knowledge of the α_2 reduction factor reflecting the incomplete alignment of the initial spins of the emitting levels. Moreover, a possible further reduction had to be considered due to the presence of isomers, as long lifetimes can affect the alignment by interactions with hyperfine fields. It is important to note that the coincidence data used in the angular- distribution analysis covered the prompt 0 - 30 ns time range only and this requirement strongly enhances prompt population of the states of interest so that, in practice, the latter effect had to be considered mainly for isomeric transitions. The A_2 coefficients obtained for most transitions did not show any significant impact from higher-lying isomers. Hence, the reduction in A_2 values consistently observed with respect to the theoretical ones resulted in the average value of $\alpha_2 = 0.65$ adopted for δ mixing ratio determinations. Note that the results for the 285-, 1413-, and 2615-keV transitions below the 10^+ isomer are also listed in Table V to demonstrate that, in this case as well, a rather small reduction of A_2 coefficients values due to the isomeric half-life is achieved when only the 0 - 30 ns time range is selected. On the other hand, the reduced A_2 value measured for the predominantly prompt 2615-keV transition must arise from the less complete spin alignment imparted to ^{208}Pb in inelastic scattering processes that contribute mainly to the population of the lowest-spin states.

The ECC results (Table IV) and angular-distribution (AD) results (Table V) will now be used in the discussion of the proposed spin-parity assignments in ^{208}Pb. For all levels up to the 6744-keV, 14^- state unique spin-parity assignments were already adopted earlier [16] and the present results mostly specify the multipolarity composition of the γ transitions involved. Apart from the new 187- and 404- keV transitions discussed above and assigned (see Table IV) as $E2$ and $M2$ decay branches from the 4611-keV 8^+ level, a number of transitions located above the 10^+ isomer could be characterized. Remarkably, the complex depopulation pattern of the 14^- state that had been recognized in earlier work [21] is fully confirmed and all spin-parity assignments are now firm. Here, the AD results uniquely assign the 1508-keV line as a $14^- \rightarrow 11^+$ $E3$ transition that competes with the 295-keV, $14^- \rightarrow 13^-$ transition of $\Delta I = 1$, mixed $M1/E2$ character that exhibits a rather large $E2$ component of 20%. In this decay of the 14^- level, the weak 643-keV $M2$ branch to the 6101-keV 12^+ level could be observed as well. It should also be emphasized that the 6449-keV, 13^- level is directly linked to the two 10^+ states by $E3$ transitions (1379 and 1553 keV) and the latter compete with two $M2$ decay branches (699, 1213 keV) to the two 11^+ levels. The $E3$ character of the 1553-keV line is supported by the AD results while the main 348-keV transition depopulating the 13^- level is firmly established as a $\Delta I = 1$, $E1$ transition by both the AD and ECC results. Most of the transitions connecting positive-parity states below the 6101-keV 12^+ level were assigned as $\Delta I = 1$ transitions of predominant $M1$ character with small $E2$ components. The latter could be precisely determined as 3% and 2% for the 340- and 865-keV transitions, respectively, and estimated to be smaller than 1% for the much weaker 351- and 680-keV ones. It has to be stressed that the present results provide firm spin-parity values for the two 11^+ states, as these

assignments were previously adopted merely on the basis of the observed γ branching [16]. The 174-keV line connecting the two 10^+ levels was established to be of $M1$ character and the AD result confirmed it to be a $\Delta I = 0$ transition. The 12^-, 6435-keV level is clearly identical with the 12^- state observed and assigned in the (e, e') experiment [18] and the $E1$ depopulating transitions to the two 11^+ levels agree with the expected decay.

Above the 14^-, 6744-keV level, which is the highest-spin state available for a one particle-hole excitation in ^{208}Pb, all spin-parity assignments are based on results from the present study. The AD results for the 1284- and 1579-keV transitions uniquely assign $I^\pi = 15^-$ to the 8027-keV level and the 1231-keV line, characterized as $\Delta I = 0$ $M1/E2$ transition, establishes the 14^- assignment to the 7974-keV state which is predominantly populated by the 53-keV unobserved $M1$ transition. Both levels are also depopulated by the weak 498- and 445-keV γ rays, respectively, which feed the non-yrast state at 7529 keV, assigned as $I^\pi = 13^-$. The 1428-keV transition depopulating this level to the 12^+, 6101-keV state shows an AD consistent with a $\Delta I = 1$ $E1$ transition, whereas the 1080-keV link to the 13^-, 6449-keV level is the only observed decay branch connecting to the lower-lying negative-parity levels. In Table II, a very weak 2634-keV γ ray from this 13^- level to the isomeric 10^+ state is listed with an intensity close to the detection limit. This transition should be viewed as tentative and is, hence, included as a dashed link in the level scheme (Fig. 4). Nevertheless, it possibly represents the $E3$ branch that one would anticipate as the result of the straightforward coupling of the 10^+ state with the 3^- core excitation that produces the 13^- level located within the 1.2-MeV energy gap separating yrast one- and two-particle-hole excitations.

The spin-parity assignments to negative-parity levels located above the 8027-keV 15^- state require taking the properties of transitions feeding those levels in the yrast decay into account. Therefore, it is useful to first settle the assignments to the 9061-, 9103-, and 9394-keV states that are predominantly populated in the main yrast sequence. The 2318-keV γ ray is clearly characterized by the AD as being of stretched $E3$ character. This results in the $I^\pi = 17^+$ assignment to the 9061-keV level. The $\Delta I = 1$, $M1$ nature of the unobserved 42-keV transition was deduced from the fact that it is the only possibility consistent with the competing γ decay to negative-parity states, thus the 9103-keV level is assigned $I^\pi = 18^+$. The 19^+ spin-parity of the 9394-keV state follows directly from the $M1$ multipolarity established by the ECC result for the 291-keV γ ray, while the AD result defines it as a $\Delta I = 1$, $M1$ transition with a ~ 2.6% $E2$ component. It may be noted that a possible competing $19^+ \rightarrow 17^+$ $E2$ cross-over branch could not be observed.

The 290-keV transition was established as a $\Delta I = 1$, $E1$ transition based on the ECC and AD results. This then results in the $I^\pi = 17^-$ assignment to the 8813-keV level, from which the yrast depopulation through lower-lying negative-parity levels is initiated. Moreover, the AD result defines the 786-keV line as a $\Delta I = 2$, $E2$ transition, an observation that strongly supports the 17^- spin-parity for the 8813-keV state. In a similar way, the ECC and AD results for the 212-keV γ ray fix the $I^\pi = 16^-$ assignment to the 8601-keV level. Whereas the contribution of unresolved transitions from several complementary Pb isotopes obscured the analysis of the 324-keV γ ray, a $I^\pi = 15^-$ assignment to the 8351-keV state could be made by considering the observed decay pattern. Furthermore, the AD result for the 250-keV transition feeding this level is consistent with this assignment. A most likely, but not unique, 15^- spin-parity assignment is proposed for the weakly-populated 8151-keV state. Also, 15^- and 16^- assignments were adopted for the respective 8265- and 8724-keV levels, as they reflect best the observed decays and a population typical of non-yrast levels.

The main population intensity feeding the yrast 9394-keV, 19^+ level proceeds via the 10342-keV isomeric state, which decays predominantly by the isomeric 948-keV transition defined by the AD result as being a $\Delta I = 1$ dipole transition. Since the $M1$ character can be safely excluded, due to the 22-ns half-life of the isomer, and since any possible $M2/E3$ mixing cannot produce the negative A_2 AD coefficient, the 948-keV γ ray has to be assigned as a $E1$ transition, and this in turn settles the $I^\pi = 20^-$ spin-parity for the 10342-keV isomer. The ECC result that favors an $E2$, but does not exclude an $E1$ assignment, for the 206-keV weak isomeric decay branch results in the proposed $I^\pi = (18^-,19^+)$ assignment to the 10136-keV state depopulated by the $E1(M1)$ 1033-keV line to the 9103-keV, 18^+ level. The even weaker 146-keV isomeric-decay branch is compatible with the $E1$ assignment (see Table IV) required by the 20^+ spin-parity of the 10196-keV level assigned based on the 802-keV transition AD result. For the remaining levels; *e.g,* those that did not exhibit any connection with higher-lying yrast states and are linked to the yrast 9394-keV level, only tentative spin-parity assignments are indicated in Fig. 4. These are based on the observed prompt population and decay paths, which favor 20^+ assignments to the 10357-, 10371- and 10531- keV levels and 19^+ to the 10136-keV one that is depopulated by the 742-keV line and is almost degenerate with, but clearly differs from, the 18^-, 10136-keV state fed by 206-keV line in the isomeric decay. In a similar way, only a tentative 20^+ assignment could be proposed for the weakly-populated 10552-keVstate. On the other hand, the relatively intense 592-keV transition is depopulating the 10934-keV level, an observation suggesting an yrast character for this state. Since no decay to positive-parity levels could be observed, the negative-parity 21^- assignment can be adopted with confidence, especially when also taking into account the absence of a decay branch feeding this state from the higher-lying 11361-keV isomer.

The notably large, positive A_2 coefficient obtained in the AD analysis for the 1019-keV transition uniquely assigns it as yet another stretched-$E3$ transition, and this establishes the $I^\pi = 23^+$ assignment for the $T_{1/2} = 13$ ns, 11361-keV isomeric state. Above this isomer, the 25^+ spin-parity assigned to the 12949-keV level is based on the stretched-$E2$ multipolarity of the 1588-keV line (Table V). As a result, the cascading 991- and 597-keV γ rays that represent the competing decay branch out of the latter level have to be of $M1$ character, herewith settling the $I^\pi = 24^+$ assignment to the intermediate state at 11958 keV. Although the well-known background from (n,n') scattering in Ge detectors obscured the AD analysis for the strongly populated 597-keV line, this prompt population was found to support the proposed assignment. The less accurate, but also large, positive A_2 coefficient obtained in the AD analysis of the 725-keV line (see Table V) favors its assignment as a stretched-$E3$ transition, as for the 1019-keV transition discussed above. As discussed earlier, a small reduction of the A_2 value can be expected for the 725-keV transition as it represents the main decay branch from the 60-ns, 13675-keV isomeric state. Thus, the $I^\pi = 28^-$ assignment to the highest-lying isomer seems well justified. Furthermore, a strong additional argument for this assignment comes from the $E2$ character inferred from the ECC result for the 139-keV transition associated with the competing branch in the 13675-keV isomer decay. This transition populates the 13536-keV state which can then be assigned $I^\pi = 26^-$ quantum numbers, herewith defining the $E1$ character of the depopulating 587-keV line to the 12949-keV, 25^+ level.

Finally, no spin-parity assignments are proposed for the levels established above the 60-ns, 13675-keV isomer (see Fig. 4). As noted in the previous section, this part of the level scheme is more tentative and certainly incomplete. However, it is noteworthy that the assumption that the four transitions placed in cascade between the isomer and the highest-

energy state at 16362 keV (Fig. 4) are all of stretched-dipole character, leads to the conclusion that the present data have extended knowledge of states in ^{208}Pb into the I = 32 angular-momentum range.

4. Discussion

A. Reduced transition probabilities

A large number of long-lived states has been identified in the high-spin level structure of ^{208}Pb. This provides an opportunity to review in a systematic way the reduced transition probabilities for isomeric transitions in this doubly-magic nucleus. The complete set of transition probabilities, calculated in Weisskopf units from the measured half-lives and the observed γ branching ratios, is listed in Table VI. The list is ordered by the increasing excitation energy and spin of the isomers and, in each case, all the transitions depopulating the isomer are included, with their respective energy, multipolarity and measured branch. In addition, Table VI includes results relevant for the decays from the 14^-, 6744- and 13^-, 6449-keV states, although, as will be explained below, estimated half-life values had to be used for both levels. As a useful reference, the reduced transition probabilities adopted in the literature for the $E3$ transition from the 2615-keV, 3^- state in ^{208}Pb [16], as well as for the $E3$ and $M2$ transitions from the $15/2^-$ level in ^{209}Pb [27] are also included at the end of Table VI.

All states in ^{208}Pb involving one particle-hole excitations are rather well understood and shell-model calculations provide insight into their detailed structural composition [23,24,28]. Therefore, the reduced transition probabilities for isomeric decays in this part of the level scheme can be interpreted while taking into account the calculated wave functions of the initial and final states. The most complex decay involves the 3.2-ns, 4611-keV 8^+ isomer with seven γ-decay branches of which five were established in the present work for the first time. As discussed in Ref. [28], the predominant amplitude (a = -0.78) of the $\nu j_{15/2}p_{1/2}^{-1}$ configuration in the 8^+ isomer structure accounts well for the 12.3 enhancement factor of the main 1413-keV, $E3$ transition to the pure (a = 0.97) $\nu g_{9/2}p_{1/2}^{-1}$ lowest 5^- level. This observation can be recognized as a first manifestation of the involvement of the fast (26 W.u.) $j_{15/2}\rightarrow g_{9/2}$ $E3$ transition seen in ^{209}Pb (see Table VI). As will be shown later, enhanced $E3$ transitions of this type feature prominently in the yrast decay of higher-spin states. The second 5^- level (3709 keV) populated by the 902-keV $E3$ transition from the 8^+ isomer has a much smaller $\nu g_{9/2}p_{1/2}^{-1}$ amplitude (a = 0.26) and, as expected, this translates into a reduced $E3$ transition probability of only 0.71 W.u. Also, the $B(M2)$ values extracted for the three $M2$ transitions from the 8^+ isomer can be understood by taking into account the structure of the 6^- states to which the decays proceed. The lowest-lying 6^- level, with a nearly pure $\nu g_{9/2}f_{5/2}$ structure, is populated by the strongly hindered 691-keV, $M2$ transition: this reflects the absence of any $M2$ connection from the predominant $\nu j_{15/2}\, p_{1/2}^{-1}$ structure of the 8^+ level. On the other hand, both higher-lying 6^- levels, populated by the 228- and 404-keV $M2$ transitions, include in their wave function sizable amplitudes for the $\nu i_{11/2}p_{1/2}^{-1}$ configuration. This in turn enables decay via a $j_{15/2}\rightarrow i_{11/2}$ $M2$ transition, such as that known in ^{209}Pb. The corresponding $B(M2)$ values (Table VI) are in the range of the transition probability established in ^{209}Pb, but they indicate a larger $\nu i_{11/2}p_{1/2}^{-1}$ wave function amplitude in the 6^-_3 level rather than in the 6^-_2 state, in contrast with expectations based on the empirical wave functions extracted in Ref. [28]. The remaining 187-keV, $E2$ and 573-keV, $E1$ transitions depopulating the 8^+ isomer are characterized by hindrance factors typical for other $E2$ and $E1$ transitions observed in ^{208}Pb.

The decay of the 10^+ isomer was extensively discussed in Refs. [26,28] and the more accurate $B(E2)$ and $B(E3)$ values reported here for the two $E2$ and one $E3$ decay branches (Table VI) do not provide new insights. Both $E2$ transitions are much slower than the corresponding single-particle values indicating a rather small amplitude in the structure of the 10^+ isomer for the $\nu j_{15/2} f_{5/2}^{-1}$ component of the wave function, that would open the $f_{5/2} \rightarrow p_{1/2}$ $E2$ (1 W.u.) decay to the two 8^+ levels of predominant $\nu j_{15/2} p_{1/2}^{-1}$ structure. It should be noted that the 34-keV $E2$ transition populating the 8^+_2 level is ten times faster than the 285-keV $E2$ branch to the 8^+_1 state and, possibly, these 8^+ levels differ more from one another than follows from the nearly identical wave functions calculated in Ref. [28]. Also, the hindrance factor (0.36) extracted for the 858-keV, $E3$ decay branch to the 7^- level of nearly pure $\nu g_{9/2} f_{5/2}^{-1}$ structure confirms a rather small $\nu j_{15/2} f_{5/2}^{-1}$ wave function amplitude in the 10^+ isomer structure.

The lifetimes of the highest-spin one particle-hole excitations; *e.g.*, the 13^- and 14^- states associated with a pure $\nu j_{15/2} i_{13/2}^{-1}$ configuration have not been determined, yet both levels exhibit rather remarkable deexcitation patterns that deserve to be discussed in a quantitative way. They are included in Table VI. The 1508-keV, $E3$ transition represents a nearly 50% decay branch from the 14^-, 6744-keV level to the final 11^+, 5235-keV state of pure $\nu g_{9/2} i_{13/2}^{-1}$ intrinsic structure. Thus, with the $i_{13/2}$ neutron-hole having no $E3$ connection to any other available neutron orbitals and, thus, acting as a spectator, the 1508-keV $E3$ transition rate was assumed to be 30 times enhanced, similarly to the $j_{15/2} \rightarrow g_{9/2}$ $E3$ rate known in ^{209}Pb (Table VI). This assumption results in an expected half-life of 0.42 ns for the 14^- level. This value was then used to calculate reduced transition rates for the other decay branches out of the 14^- state. The 295-keV $M1/E2$ transition, with a 20% $E2$ admixture determined from the AD results, represents a slow (6×10^{-4} W.u.) $M1$ transition, while the $E2$ component of 0.61 W.u. appears to be rather fast for ^{208}Pb. The $B(M1)$ rate is expected to be proportional to the squared difference of the g-factors for the $j_{15/2}$ and $i_{13/2}^{-1}$ neutron orbitals: the low rate is a natural consequence of both g-factor values being small and similar. This decay was extensively discussed in Ref. [21], however, the present results provide a more detailed input, excluding also the expectation that the 295-keV transition could be predominantly of $E2$ character. On the other hand, the 643-keV $M2$ transition discussed in Ref. [21] was observed in the present measurements and the extracted probability of $B(M2) = 0.35$ W.u. is close to the ^{209}Pb $M2$ rate, herewith confirming the $\nu i_{11/2} i_{13/2}^{-1}$ predominant configuration for the 12^+, 6101-keV level. In addition, the intensity limit established for the unobserved 994-keV, $E3$ transition from the 14^- level to the 11^+_2, 5750-keV state defines the upper limit of 4 W.u. for this $E3$ rate. This value largely excludes the $\nu g_{9/2} i_{13/2}^{-1}$ amplitude in the wave function of the final state.

A similar approach can also be adopted for the 13^-, 6449-keV level, where the decay involves two $E3$ branches to the two 10^+ levels with similar transition rates. In this case, the nearly equal sharing of the $\nu g_{9/2}\, i_{13/2}^{-1}$ wave function amplitude between both 10^+ levels justifies the assumption that the 1553-keV transition takes only half of the ^{209}Pb $E3$ strength (*i.e.,* 15 W.u.). This in turn results in a 0.19-ns half-life estimate for this 13^- state (Table VI). The 1379-keV, *E3* transition is then 17 times enhanced, while the 699-keV $M2$ transition with its 0.44 W.u. rate is close to the ^{209}Pb $M2$ rate, an observation confirming the role of the $\nu i_{11/2} i_{13/2}^{-1}$ configuration in the wave function of the 11^+_2, 5750-keV final state. The order of magnitude smaller $B(M2)$ rate for the 1213-keV γ ray to the 11^+_1 level indicates that such a $\nu i_{11/2} i_{13/2}^{-1}$ amplitude is negligible in the wave function of the latter state. Finally, the main 348-keV $E1$ branch from the 13^- level exhibits a 10^5 hindrance factor, a typical value for $E1$ transitions.

The three isomeric states in the high-spin part of the ^{208}Pb level scheme must involve more complex multi-particle-hole configurations which, at present, are not yet understood to the extent that the observed decay paths can be interpreted in a complete way similar to those proposed above. Nevertheless, the extracted transition rates can provide hints useful for the improvement of shell-model calculations. The 22-ns, 20^- isomer at 10342 keV decays by two $E1$ transitions with typical retardation factors in the $10^7 - 10^8$ range, and one $E2$ γ ray with a 0.046 W.u. rate similar to that of several other $E2$ transitions seen in the lower part of the level scheme. Note that the possibility discussed above that the latter transition (206 keV) be of $E1$ character would result in it being a factor of 3 slower than the 146-keV $E1$ γ ray. All of these rates are in line with the transition multipolarity assignments, but do not clarify details of the initial and final state wave functions. More interesting is the case of the 13-ns, 23^+ isomer at 11361 keV which is depopulated by a single, 1019-keV $E3$ transition with $B(E3)$ = 32 W.u. This enhancement is similar to the corresponding $E3$ rate in ^{209}Pb, an observation that strongly suggests that the $\nu\, j_{15/2} \rightarrow g_{9/2}$ transition plays a main role in this fast $E3$ decay. Consequently, the structure of the 23^+ and 20^- isomeric states must involve the $j_{15/2}$ and $g_{9/2}$ neutron orbitals, respectively.

Finally, the decay of the highest-spin 28^- isomer at 13675 keV ($T_{1/2}$ = 60 ns) appears to be the most puzzling. Whereas, the 139-keV $E2$ decay branch with its 0.21 W.u. rate falls within the range of other $E2$ rates observed in ^{208}Pb, the 725-keV $E3$ γ ray, with B($E3$) = 56 W.u., has to be recognized as being among the fastest $E3$ transitions ever observed. A maximum spin value of I = 26 can be achieved with the available two-particle two-hole excitations in ^{208}Pb. Thus, this 28^- isomer must necessarily involve at least one additional particle-hole excitation. Although the intrinsic structure of this long-lived level is likely complex and beyond the scope of the present paper, it can be speculated that the involvement of two $j_{15/2}$ neutrons in the configuration of the 28^- isomer may well be necessary to account for the remarkably fast $E3$ transition to the $g_{9/2}$ neutrons involved in the wave function of the final 25^+ state. A more detailed understanding of this fast $E3$ transition probably requires significant progress in shell-model calculations.

Summarizing this section, it is worth to review the general situation with regards to $E3$ transitions. Quite a few of these are present in the ^{208}Pb yrast decay from the highest-spin levels down to the ground state. In all, eleven $E3$ transitions could be observed and they fall into three categories. The first involves the 2615-, 2318- and 2634-keV transitions and is associated with the collective 3^- ^{208}Pb core excitation coupled to the ground state, the 14^-, 6744-keV level, and the 10^+, 4895-keV isomer, respectively. In the second category, the 902- and 858-keV $E3$ transitions can be placed. They depopulate the 8^+ and 10^+ isomers, respectively, and do not appear to show any sign of collectivity, with $B(E3)$ values well below the Weisskopf unit. Here, also the unobserved 994-keV $E3$ branch from the 14^- level may be included with its established upper limit for the $B(E3)$ probability. All of the six remaining $E3$ transitions with energies of 725, 1019, 1379, 1413, 1508, and 1553 keV are strongly enhanced due to the involvement of the $\nu j_{15/2} \rightarrow g_{9/2}$ fast $E3$ transition known from the data in ^{209}Pb. It is possible, and perhaps even likely, that the double involvement of this transition is responsible for the factor of 2 enhancement in the $E3$ rate of the 725-keV transition which would be anticipated in the event of a double octupole phonon excitation.

Shell-model calculations and interpretation of high-spin levels

Shell-model calculations were carried out with the OXBASH code [29], including all 24 orbitals comprising the four major shells surrounding ^{208}Pb, as described in detail in Ref. [23]. The calculations involved a basis of 1p-1h and 2p-2h states arising from all possible combinations of orbitals available for proton-hole ($1g_{7/2}$, $2d_{5/2}$, $2d_{3/2}$, $3s_{1/2}$, $1h_{11/2}$), proton-particle ($1h_{9/2}$, $2f_{7/2}$, $2f_{5/2}$, $3p_{3/2}$, $3p_{1/2}$, $1i_{13/2}$), neutron-hole ($1h_{9/2}$, $2f_{7/2}$, $2f_{5/2}$, $3p_{3/2}$, $3p_{1/2}$, $1i_{13/2}$) and neutron-particle ($1i_{11/2}$, $2g_{9/2}$, $2g_{7/2}$, $3d_{5/2}$, $3d_{3/2}$, $4s_{1/2}$, $1j_{15/2}$) excitations. The particle-hole two-body matrix elements (TBME) were obtained from the M3Y potential calculated with harmonic-oscillator radial wave functions.

There are two approximate ways to carry out these calculations. The one labeled (2016) was obtained with pure Np-Nh configurations. The single-particle energies for the 24 orbitals relative to ^{132}Sn were adjusted to reproduce the experimental energy differences given in Ref. [28] based upon a closed-shell configuration of ^{208}Pb, a closed-shell plus one particle for A = 209, and closed shell plus one hole for A = 207. The spectra of the 1p-1h, 2p-2h, and 3p-3h states were then calculated independently. The 3p-3h model space was truncated by keeping the (deep) proton $1g_{7/2}$ and neutron $1h_{9/2}$ orbitals filled and leaving out the (low-spin) proton $3p_{3/2}$ and $3p_{1/2}$ as well as the neutron $3d_{3/2}$ and $4s_{1/2}$ states. The calculations labeled (2000) are from Ref. [23]. The emphasis in the latter work was on coupling the 2p-2h and 1p-1h states in order to study double-octupole excitations and, as discussed in [23], this involved several complications. The wave functions of A = 209 were obtained from a 1p plus 2p-1h basis and the wave functions for A = 207 were obtained in a 1h plus 1p-2h basis. The 24 single-particle energies were adjusted to reproduce the (A = 209) - (A = 208) and (A = 208) - (A = 207) energy differences. The energies of the 2p-2h states in ^{208}Pb had to be shifted down by 2.1 MeV to account for the truncation in the Np-Nh series (*i.e,* the lack of 3p-3h and higher-N states) It is difficult to extend the (2000) calculations beyond 2p-2h for ^{208}Pb. On the other hand, it is easy to extend the (2016) calculations to 3p-3h states, since the single-particle energies do not have to be readjusted with each change of the model space.

Here, results of the calculations will be restricted to yrast and near-yrast states that can be compared with the observed experimental levels as displayed in the low-spin (Fig. 2) and high-spin (Fig. 4) parts of the ^{208}Pb level scheme. Thus, Figs. 12 and 13, respectively, compare the energies of these low-spin and high-spin data with those obtained in the two shell-model calculations described above and labeled as 2000 (left) and 2016 (right). The understanding of the 1p-1h states displayed in Fig. 12 and extending up to the highest-spin 14^- level at 6744 keV is rather complete and has been broadly discussed in Refs. [17,21,28] as well as in the most recent work by Heusler et al. [24]. The new data presented in this work provided more detailed information on the γ-decay paths out of several states. In essence, they confirm the state wave functions established previously, as was extensively discussed in Sec. 3A. Also, the quantitative comparison between the calculated and experimental level energies of Fig. 12 demonstrates a satisfactory reproduction of the data by both calculations, except for the somewhat larger deviations observed for the 6^+ and 12^+ levels. It has to be kept in mind that, in general, the close agreement is valid mostly for the yrast and near-yrast states for which the structure is usually better defined. Nevertheless, the energies of the first three levels observed in the experiment with $I^\pi = 5^-$, 6^-, and 9^+ are also rather well reproduced by the calculations.

More relevant for the present study is the comparison (Fig. 13) between experimental and calculated level energies in the high-spin part of the ^{208}Pb scheme; *i.e*., above the 10^+ isomer (Fig. 4). Note that Fig. 13 also includes the three highest-spin, 1p-1h states, which extend up to the 14^- level at 6744 keV, herewith demonstrating on the energy scale of Fig. 13 the

agreement between data and both calculations. All the calculated states above this 14^- level correspond to 2p-2h excitations which extend up to the maximum spin value of $I = 26$. Above this spin, 3p-3h or higher-order excitations need to be considered and those levels, which could be calculated only within the (2016) approach, are framed in a separate box to emphasize that they were calculated using the truncated configuration space. Starting with the $I = 14$ level, for each spin and parity, the three lowest-lying states were calculated. Yet, for clarity, only those which can be matched with an experimental counterpart are presented in Fig. 13. Note also that, as in Fig. 12, for ease of comparison between experimental and calculated level energies, positive- and negative-parity states are displaced in the figure. Within the 1.2 MeV energy gap above the 1p-1h, 14^- excitation, only one, distinctly non-yrast, 13^- level was observed at 7529 keV. Whereas both calculations predict the 13^- level around this energy, the presence of the 2634-keV depopulating transition of $E3$ multipolarity to the 10^+ isomer (see Table II) indicates an intrinsic structure involving the 10^+ isomer wave function coupled to the 3^- ^{208}Pb core excitation.

For both the (2000) and (2016) calculations, a satisfactory agreement is observed for the group of experimental and calculated negative-parity levels with $I^\pi = 14^-$, 15^-, 16^-, and 17^-. However, the more detailed comparison of theoretical and experimental levels will be focused on the (2016) calculations which, in general, agree better with experiment and also more readily provide insight into the calculated wave functions. In the above group of negative-parity states, one notices that, whereas the fragmented wave functions of the 14^- and three 15^- states involve the $\pi h_{9/2}h_{11/2}^{-1}\nu g_{9/2}\, p_{1/2}^{-1}$ configuration with amplitudes <55%, the two 16^- and one 17^- levels are predominantly of $\pi h_{9/2}h_{11/2}^{-1}\nu g_{9/2}f_{5/2}^{-1}$ character. For example, the corresponding amplitude for the 17^- state amounts to 81%. The experimental positive-parity levels with $I^\pi = 17^+$, 18^+, and 19^+ are also rather well matched with their calculated counterparts. Their calculated energies establish the yrast character of these states, herewith confirming the main yrast decay path observed in the experiment. Here, the experimental 17^+ state at 9061 keV is reproduced within 15 keV with the calculations resulting in a higher energy and, as anticipated above, the fragmented wave function of this level involves the $\nu j_{15/2}i_{13/2}^{-1}$ 1p-1h excitation coupled to the collective 3^- core excitation with the associated small (<15%) amplitudes. It should be mentioned that a similarly good agreement (26 keV below experiment) is obtained when the energy of the 17^+ level is calculated by combining the shifts of the observed particle-octupole couplings of the individual $\nu j_{15/2}$ (in ^{209}Pb) and $\nu i_{13/2}^{-1}$ (in ^{207}Pb) orbitals, as considered in Refs. [15,21]. The 19^+ yrast state is computed to be 137 keV higher than the experimental energy and the predominant wave function amplitude (94%) corresponds to the $\pi h_{9/2}h_{11/2}^{-1}\nu g_{9/2}\, i_{13/2}^{-1}$ configuration. On the other hand, the theoretical yrast 18^+ level is calculated nearly 300 keV too high in excitation energy with a 61% wave-function amplitude belonging to the $\pi h_{9/2}h_{11/2}^{-1}\nu j_{15/2}\, p_{1/2}^{-1}$ configuration. The next 18^+ state is characterized by a wave function dominated by the same main configuration as the 19^+ state above (73% amplitude), but is calculated 400 keV higher in excitation energy than the experimental yrast 18^+ level. Nevertheless, the data favor an interpretation involving this computed state as corresponding to the observed one, based on the observation that the yrast flux proceeds almost completely between the 19^+ and 18^+ levels.

Above the 19^+ level, comparisons between observed and computed states become less straightforward, and the matching of data and calculations may well be fortuitous in some instances. Specifically, the relatively simple yrast decay path observed in the measurements cannot be readily inferred from the calculated results.

The 20^-, 10342-keV isomeric state is fairly well matched with the 20^- level calculated at 10526 keV that is characterized by a predominant (91% wave-function amplitude) $\pi i_{13/2} h_{11/2}^{-1} \nu g_{9/2} i_{13/2}^{-1}$ configuration. However, the three predicted 20^+ levels would be yrast as they are computed to be 0.5 - 1 MeV lower in energy, a situation that is not confirmed by the experimental location of such states. The five 20^+ states established in the experiment are much closer in energy to the 20^- isomer and three of these are relatively strongly populated, as would be expected for levels competing for yrast status. This situation accounts for the observation of a strongly populated 20^- isomeric state and, in fact, this level would hardly have been detected if the energies of the 20^+ levels had been as low as the computed ones. Indeed, in such a theoretical scenario, the 20^- state population would have been substantially reduced, and the isomerism itself might not have been present as much faster decay out paths would have been enabled. Also, the 21^- level of predominantly the same configuration as the 20^- state is calculated to be close in energy (48 keV), in contrast to the experimental 21^- candidate that is located nearly 600 keV above the 20^- isomer. Although the energies of the three 20^+ levels calculated within the (2000) approach and shown to the left in Fig. 13 are much closer to the experimental counterparts, the calculated 20^- and 21^- levels are much too high in energy to be populated in the yrast decay and, in particular, also these calculated results cannot explain the existence of the 20^- isomer.

The calculated positive-parity levels with $I^\pi = 23^+$, 24^+, 25^+, and 26^+ are all associated with a pure $\pi i_{13/2} h_{11/2}^{-1} \nu j_{15/2} i_{13/2}^{-1}$ configuration as the wave-function amplitudes are close to 100%. Although in both calculations all of these levels are calculated within a narrow 300 keV range, they are located at excitation energies differing by more than 1 MeV. As a result, they can hardly be correlated with the more spread out experimental energies of the $I^\pi = 23^+$, 24^+, and 25^+ states. Any agreement between theory and experiment may well be accidental and, in particular, the 26^+ level of the same configuration, which is computed to be clearly yrast, is not even observed in the experiment. On the other hand, the lowest member of this group of states, the 23^+ level, is calculated to be located nearly 600 keV higher in energy than the well-established 23^+, 11361-keV isomer, although its computed structure agrees well with the observed *E*3 isomeric decay. Indeed, the main components of the calculated wave functions of the 23^+ and 20^- states account for the enhancement of the 1019-keV *E*3 (32 W.u.) isomeric transition that is attributed to the involvement of the $\nu j_{15/2} \rightarrow g_{9/2}$ transition in this decay (see above).

The spin-parity $I^\pi = 26^-$ and 28^-, assigned respectively to the 13536-keV level and to the highest-energy isomer at 13675 keV, require the involvement of 3p-3h excitations. Indeed, the (2016) shell-model calculations, which are extended to include 3p-3h excitations, predict such two states at reasonably close energies. However, in view of general difficulties encountered in comparisons of calculated and experimental 2p-2h high-spin excitations, any assignment of a structure to these states would be speculative, and at present one may only indicate that both 26^- and 28^- levels, as well as practically all of the 3p-3h calculated states displayed in Fig. 13, involve two-neutron and one-proton particle-hole excitations. Nevertheless, as discussed above, an important hint for future discussions is provided by the remarkable enhancement of the *E*3 isomeric transition. It is of a magnitude anticipated for the decay of a double-octupole phonon excitation. One may, thus, speculate that the $\nu j_{15/2} \rightarrow g_{9/2}$ *E*3 transition plays an essential role in this context, but further progress in shell-model calculations of ^{208}Pb high-spin states is needed to clarify the issue.

A discussion of the states above the 28^- isomer would be even more speculative, as the level sequence established in this region is only tentative (see above). The results obtained in the

present work were included mainly to demonstrate the potential of modern γ-ray spectroscopy: at present, ^{208}Pb levels up into the $I \sim 32$ range are within reach. Further exploration of this region will be challenging for both experiment and theory and simultaneous efforts on both fronts are highly desirable.

C. The yrast line and "rotation" of ^{208}Pb

For spherical quantal systems, orientations of the intrinsic frame that differ by a rotation about the symmetry axis cannot be distinguished. As a result, collective rotations will be absent from any quantal description of spherical nuclei. On the other hand, in such nuclei, high-spin states are the result of the coupling of the spin vectors of a number of nucleons; *i.e.,* these protons and/or neutrons act collectively to generate a total angular momentum that can then be attributed to a state of the entire nucleus. In this sense, this collective behavior can perhaps be viewed as a "rotation" of the system. At the same time, the nucleons in high-j orbits that couple to generate a specific spin value are also in constant interaction with other nucleons – specifically, through collisions where the occupation of orbits can change, herewith generating other excitations involving state mixing. In any event, the "rotation" of a few coupled nucleons with a significant angular momentum around the total spin axis may be converted by these interactions into a collective "rotation" of a significant part of the nucleus.

In order to test the potential of such a naive "rotational" interpretation of high-spin states in spherical ^{208}Pb, the energies of the yrast and near-yrast levels reported above are plotted versus the conventional $I(I+1)$ product in Fig. 14. The points delineating the yrast line between spins $I \sim 10$ and $I \sim 28$ follow rather well the straight line expected within a rotational picture and a fit of the states within this range with the expression for the rotational energy $E(I) = E_0 + \hbar^2/2I_{moi}\ I(I+1)$ translates into $E(I) = 4.4 + 0.013\ I(I+1)$ MeV. The slope parameter in this expression then provides the value of the moment of inertia I_{moi} of the "rotating" body, while the 4.4 MeV energy at spin $I = 0$ can be viewed as the magnitude of the shell gap required to access the free configuration space and enable the collective nuclear excitations under consideration.

It is worth noting that, in fact, the well-known single-particle energies relevant for ^{208}Pb define the gap energy to be close to 5.0 MeV and, with this value, a subsequent fit of the yrast line results in the line given in Fig. 14 and the expression $E(I) = 5 + 0.0113\ I(I+1)$ MeV. This calculated slope is larger by more than a factor of 2 than the one expected based on the rigid body moment of inertia of a rotating ^{208}Pb sphere. Thus, in addition to the fairly linear behavior with $I(I+1)$, the "rotational" interpretation also requires an understanding of the factor of 2 reduction of the actual I_{moi} value implied by the slope. In contrast to the situation in deformed nuclei, pairing cannot be responsible for this reduction as pairs are broken in particle-hole excitations needed to initiate the "rotation". One way to look at the observation is to consider whether the "rotation" should be attributed to the entire spherical nucleus, or possibly only to a part of it. A priori, one would anticipate that nucleons occupying deeply-bound orbitals can be excluded from participation in such a collective motion as an additional - rather high - energy would be required for them to access the free configuration space of interest. Thus, the "rotation" could possibly involve only the weaker-bound nucleons; *e.g.*, those located in external layers of the nucleus. Assuming that ^{208}Pb consists of a ^{132}Sn inert spherical core that does not participate in the rotation, and 76 additional nucleons behaving collectively reduces the rigid body moment of inertia to a value lower by a factor 0.53 than that of the whole ^{208}Pb nucleus; thus a value close to that derived from the fit of the yrast line. Interestingly, the picture in which only the external layer of ^{208}Pb rotates and the inert ^{132}Sn

sphere is not involved also agrees with the choice of the configuration space used in the shell-model calculations discussed above where the orbitals in ^{132}Sn below $Z = 50$ and $N = 82$ were not considered.

In Fig. 14, the four states above the 28^- isomer have also been included. They are placed in brackets to indicate that their spins were not assigned in the present work. In the figure, the tentative spin values conservatively assume a cascade of four yrast transitions of stretched-$M1$ character. These points were included to check whether the yrast line at the highest spins is characterized by a smaller slope and, thus, a larger moment of inertia. Although, at present, the picture is not conclusive, due to the lack of firm experimental information on spins and parity, the data suggest that a larger number of nucleons may well be involved in the "rotation" in this higher angular momentum regime. Hence, the challenging task of extending experimentally level sequences in ^{208}Pb above the 28^- isomer appears well founded.

4. Conclusions

High-spin states in ^{208}Pb have been studied in γ–γ coincidence measurements following deep-inelastic reactions involving mostly the ^{48}Ca + ^{208}Pb, and ^{208}Pb + ^{208}Pb systems, but several others as well. An elaborate level scheme, extending to more than 16 MeV in excitation energy and reaching a spin range of $I \sim 32$, was delineated. This scheme also includes considerable new experimental information in parts studied previously. Exploiting delayed coincidence techniques, three new isomers as well as levels fed by prompt radiation were firmly located and a group of transitions could be identified for the first time above the highest-spin $I^\pi = 28^-$ long-lived state. Up to the 28^- isomer, spin-parity quantum numbers could be assigned to most of the observed states on the basis of the measured angular distributions and of the total electron-conversion coefficients deduced based on intensity-balance considerations for low-energy (< 405 keV) transitions. The measured isomeric half-lives enabled the extraction of reduced transition probabilities. The latter were discussed considering the intrinsic structure of the levels involved.

A particular emphasis was placed on the $E3$ transitions that not only occur remarkably often along the yrast decay sequence, but also display features that point directly to the wave functions of the states involved. Among the noteworthy observations figure six strongly-enhanced $E3$ transitions, which appear to mirror the enhanced $\nu j_{15/2} \rightarrow g_{9/2}$ $E3$ transition known in ^{209}Pb. The largest enhancement (56 W.u.) was observed for the isomeric transition depopulating the 28^- isomer and it was tentatively proposed to indicate the involvement of a double octupole phonon excitation in the structure of this state.

Shell-model calculations were performed for ^{208}Pb that include all 1p-1h and 2p-2h excitations as well as 3p-3h states obtained within a limited configuration space. The results were compared with the data. The satisfactory agreement between experiment and theory observed for the 1p-1h excitations also extends to most of the high-spin levels associated with 2p-2h excitations and selected 3p-3h states. Based on the calculated wave functions, the interpretation of the observed levels was broadly discussed in terms of the measured decay properties. Some discrepancies between experiment and theory were found to occur in the highest part of the level scheme. It is hoped that the present study will provide guidance to improve the shell-model calculations which might in the future be extended to involve yet higher-spin states.

A "rotational" interpretation of the yrast and near-yrast states in ^{208}Pb was considered, based on the noted approximate linear dependence when the level energies are plotted versus the conventional $I(I+1)$ product. Within this picture, admittedly rather extreme for a doubly-magic nucleus, the moment of inertia was found to be a factor 2 smaller than the value expected for a rigid ^{208}Pb sphere. This observation appears to be quantitatively consistent with an interpretation where the strongly-bound ^{132}Sn core does not participate in a collective "rotation" that only involves the 76 less-bound, valence nucleons.

Acknowledgments

The authors thank the ATLAS operating staff for the efficient running of the accelerator during the long series of experiments performed for the present study and J. P. Greene for target preparations. Contributions by researchers who participated in the early phases of this study, which were reported in earlier publications, are gratefully acknowledged. This work was supported by the Polish National Science Center, Projects No. UMO-2012/07/N/ST2/02861, the U.S. Department of Energy, Office of Science, Office of Nuclear Physics, under Contract No. DE-AC02-06CH11357 (ANL) , and Grant No. DE-FG02-94ER40834 (UM), NSF Grant PHY-1404442 and the Science and Technology Facilities Council (STFC), UK. This research used resources of ANL's ATLAS facility, a DOE Office of Science User Facility.

References

[1] G. H. Herling, T. T. S. Kuo, Nucl. Phys. A **181**, 113 (1970);
T. T. S. Kuo, G. H. Herling, US Naval Research Laboratory Report Nr. 2258, 1971 (unpublished).
[2] E. K. Warburton, and B. A. Brown, Phys. Rev. C **43**, 603 (1991).
[3] L. Corragio, A. Covello, A. Gargano, N. Itako, T. T. S. Kuo, Phys. Rev. C **60**, 064306 (1999).
[4] R. Broda, J. Phys. G: Nucl. Part. Phys. **32**, R151 (2006).
[5] B. Szpak, K.H. Maier, A. S. Smółkowska, B. Fornal, R. Broda, M. P. Carpenter, N. Cieplicka, R. V. F. Janssens, W. Królas, T. Pawłat, J. Wrzesiński, and S. Zhu, Phys. Rev. C **83**, 064315 (2011).
[6] J. Wrzesiński, G. J. Lane, K. H. Maier, R. V. F. Janssens, G. D. Dracoulis, R. Broda, A. P. Byrne, M. P. Carpenter, R. M. Clark, M. Cromaz, B. Fornal, T. Lauritsen, A. O. Macchiavelli, M. Rejmund, B. Szpak, K. Vetter, and S. Zhu, Phys. Rev. C **92**, 044327 (2015).
[7] R. Broda, K. H. Maier, B. Fornal, J. Wrzesiński, B. Szpak, M.P. Carpenter, R. V. F. Janssens, W. Królas, T. Pawłat, and S. Zhu, Phys. Rev. C **84**, 014330 (2011)
[8] J. Wrzesiński, R. Broda, B. Fornal, W. Królas, T. Pawłat, M.P. Carpenter, R.V.F. Janssens, D. Seweryniak, S. Lunardi, C.A. Ur, G. Viesti, M. Cinausero, N. Marginean, and K. H. Maier, Eur. Phys. J. A **20**, 57 (2004).
[9] N. Cieplicka, K. H. Maier, B. Fornal, B. Szpak, R. V. F.Janssens, M. Alcorta, R. Broda, M. P. Carpenter, C. J. Chiara, C. R. Hoffman, B. P. Kay, F. G. Kondev, W. Królas, T. Lauritsen, C. J. Lister, E. A. McCutchan, T. Pawłat, A. M. Rogers, D. Seweryniak, N. Sharp, W. B. Walters, J. Wrzesiński, and S. Zhu, Phys. Rev. C **86**, 054322 (2012).
[10] M. Schramm, H. Grawe, J. Heese, H. Kluge, K. H. Maier, R. Schubart, R. Broda, J. Grębosz, W. Królas, A. Maj, and J. Blomqvist, Z. Phys. A **344**, 121 (1992)
[11] M. Rejmund, K. H. Maier, R. Broda, B. Fornal, M. Lach, J. Wrzesiński, J. Blomqvist, A. Gadea, J. Gerl, M. Gorska, H. Grawe, M. Kasper, H. Schaffner, C. Schlegel, R. Schubart, and H. J. Wollersheim, Eur. Phys. J. A **1**, 261 (1998).
[12] M. Rejmund PhD Thesis GSI DISS 99-03 (1999).
[13] B. Fornal, R. Broda, K.H. Maier, J. Wrzesiński, G. J. Lane, M. Cromaz, A. O. Macchiavelli, R. M. Clark, K. Vetter, A. P. Byrne, G. D. Dracoulis, M. P. Carpenter, R. V. F. Janssens, I. Wiedenhoever, M. Rejmund and J. Blomqvist, Phys. Rev. Lett. **87**, 212501 (2001).
[14] G. D. Dracoulis, P. M. Walker, and F. G. Kondev, Rep. Prog. Phys. **79**, 076301 (2016)
[15] M. Rejmund, K. H. Maier, R. Broda, B. Fornal, M. Lach, J. Wrzesiński, J. Blomqvist, A. Gadea, J. Gerl, M. Gorska, H. Grawe, M. Kaspar, H. Schaffner, C. Schlegel, R. Schubart, and H.J. Wollersheim, Eur. Phys. J. A **8**, 161 (2000).
[16] M.J. Martin, Nucl. Data Sheets **108**, 1583 (2007).
[17] M. Schramm, K. H. Maier, M. Rejmund, L. D. Wood, N. Roy, A. Kuhnert, A. Aprahamian, J. Becker, M. Brinkman, D. J. Decman, E. A. Henry, R. Hoff, D. Manatt, L. G. Mann, R. A. Meyer, W. Stoeffl, G. L. Struble, and T. -F. Wang, Phys. Rev. C **56**, 1320 (1997).
[18] J. P. Connelly, D. J. de Angelis, J. H. Heisenberg, F. W. Hersman, W. Kim, M. Leuschner, T. E. Millimann, J. Wise, and C. N. Papanicolas, Phys. Rev. C **45**, 2711 (1992).
[19] M. Schramm, H. Grawe, J. Heese, H. Kluge, K. H. Maier, R. Schubart, R. Broda, J. Grębosz, A. Maj, and J. Blomqvist, Z. Phys. A **344**, 363 (1993).

[20] R. Broda, J. Wrzesiński, T. Pawłat, B. Fornal, Z. Grabowski, D. Bazzacco, S. Lunardi, C. Rossi-Alvarez, G. de Angelis, A. Gadea, and K. H. Maier, *Proceedings of the Conference on Nuclear Structure at the Limits*, Argonne, Illinois, July 1996. ANL/Phy-97/1, p.276
[21] J. Wrzesiński, K. H. Maier, R. Broda, B. Fornal, W. Królas, T. Pawłat, D. Bazzacco, S. Lunardi, C. Rossi-Alvarez, G. de Angelis, A. Gadea, J. Gerl, and M. Rejmund, Eur. Phys. J. A **10**, 259 (2001).
[22] R. Broda, B. Fornal, W. Królas, T. Pawłat, J. Wrzesiński, D. Bazzacco, G. de Angelis, S. Lunardi, and C. Rossi-Alvarez, Eur. Phys. J. A **20**, 145 (2004).
[23] B. Alex Brown, Phys. Rev. Lett. **85**, 5300 (2000)
[24] A. Heusler, R. V. Jolos, T. Faestermann, R. Hertenberger, H. -R. Wirth, and P. von Brentano, Phys. Rev. C **93**, 054321 (2016).
[25] I. Y. Lee, Nucl. Phys. A **520**, 641c (1990).
[26] N. Roy, K. H. Maier, A. Aprahamian, J. A. Becker, D.J. Decman, E. A. Henry, L. G. Mann, R. A. Meyer, W. Stoeffl, and G. L. Struble, Phys. Lett. B **221**, 6 (1989).
[27] J. Chen and F.G. Kondev, Nucl. Data Sheets **126**, 373 (2015).
[28] M. Rejmund, M. Schramm, and K. H. Maier, Phys. Rev. C **59**, 2520 (1999).
[29] B. A. Brown, A. Etchegoyen, W. D. M. Rae, N. S. Godwin, W. A. Richter, C. H. Zimmerman, W. E. Ormand, and J. S. Winfield, MSU-NSCL Report No. 524, (1985).

Table Captions – 208Pb

I. List of low-spin (≤10) yrast and near-yrast ^{208}Pb states together with the depopulating transitions observed in the present study and displayed in Fig. 2. The level energies and I^{π} values are listed with the depopulating transition energies, associated multipolarities, and final level I^{π} values. Energy uncertainties are below 0.1 keV. The relative transition intensities reflect prompt and delayed populations, respectively (see text for details).
   a) Levels for which only the main depopulating transitions are listed (for a complete list see Ref. [15]);
   b) New transitions identified in the present work;
   c) Relative prompt intensities were estimated from cross-coincidence relationships with transitions from complementary ^{207}Pb and lighter Pb isotopes;
   d) Unobserved *E*3 transition; the upper intensity limit was estimated in order to compare with the *E*3 decay of the 8^{+}_{1} level (see text);
   e) Unobserved transition; total intensity deduced from the intensity balance.

II. List of high-spin levels and depopulating transitions observed in ^{208}Pb above the 10^{+}, 4895-keV isomer (the level scheme is given in Fig. 4). The format of the table is the same as in Table I. The prompt and delayed transition intensities are in each case normalized to the 100 units adopted for the most intense transition of 340.2 keV (see text for details). Transition multipolarities inferred only from level assignments are placed in parentheses. Level energies are determined to 0.1 keV accuracy, unless indicated.
   a) Unobserved *E*3 transition; the estimated upper intensity limit enables the comparison with the 1508-keV *E*3 decay rate (see Table VI);
   b) Unobserved low-energy transitions for which the presence was established and total (γ + ECC) intensity extracted from the coincidence data;
   c) Transitions for which the prompt component was not detected. Values listed as prompt intensity are fractions of delayed intensity observed within the prompt time window.

III. List of transitions identified in ^{208}Pb above the 28^{-} isomer at 13675 keV using coincidence data from the ^{208}Pb + ^{208}Pb and ^{48}Ca + ^{208}Pb reactions as described in text. The prompt transition intensities are normalized to the 100 units adopted for the most intense transition at 341.3 keV and listed separately for both experiments to signal a possible difference in the high-spin state population (see text for details).

IV. The total electron-conversion coefficients (ECC) extracted from intensity balances for low-energy transitions in ^{208}Pb. In the last column, the theoretical ECC values are included only for the multipolarities reflecting the experimental values (see text). For mixed *M*1+*E*2 transitions, theoretical values were calculated using δ mixing ratios extracted from angular distribution data (Table V).

V. Angular distribution results for transitions in ^{208}Pb above the 10^{+}, 4895-keV isomer and three selected transitions below it (a). The respective columns include the transition and initial level energies, the spin-parity assignments for the initial and final states, the numerical values of the fitted A_2 and A_4 angular distribution coefficients and the adopted transition multipolarity. The absence of an A_4 value indicates an instance where the fit included only the A_2 term. In the last column, the δ mixing ratios are listed for *M*1/*E*2 mixed transitions. These were obtained

taking into account the $\alpha_2 = 0.65$ coefficient adopted as reflecting the incomplete alignment of nuclear spins (see text for details).

VI. Experimental reduced transition probabilities extracted for transitions depopulating the isomeric levels in ^{208}Pb. In the respective columns, the energies, spin-parity quantum numbers and half-lives of the isomers are listed, as are the energies of the depopulating transitions with their respective multipolarity and branching intensity. The last column provides numerical values for the transition probabilities in Weisskopf units (see text for details).
   a) Half-life value from Ref. [26];
   b) Half-life is an average from determinations in Ref. [26] and the present work;
   c) The half-life was not measured, but calculated assuming the enhancement expected for the *E*3 transitions being considered (see text). Two such states are listed separately to distinguish them from those with measured half-lives;
   d) Branching for *M*1 and *E*2 components were obtained from the angular distribution results (Table V);
   e) Taken from Refs. [27] for ^{209}Pb and [15] for ^{208}Pb.

TAB.1

E_{level} [keV]	I^{π}	E_{gamma} [keV]	multipolarity	I^{π} final	In beam intensity	Offbeam intensity
0 g.s.	0^+					
2614.5	3^-	2614.5	E3	0^+	388.0 [c]	100.0
3197.7	5^-	583.2	E2	3^-	340.0 [c]	100.0
3475.1	4^-	277.4	M1+E2	5^-	18.1(7)	
		860.6	M1+E2	3^-	36.4(14)	
3708.5 [a]	5^-	510.7	M1+E2	5^-	105(3)	4.83(12)
3920.0	6^-	211.5	M1+E2	5^-	31.7(15)	2.25(7)
		722.3	M1+E2	5^-	42.2(21)	3.16(8)
3961.2 [a]	5^-	252.8	M1+E2	5^-	3.7(6)	
		763.4	M1+E2	5^-	7.3(8)	0.08(3)
4037.4	7^-	117.5	M1+E2	6^-	9.0(9)	1.1(2)
		839.7	E2	5^-	90.4(35)	11.7(3)
4206.3	6^-	497.9	M1+E2	5^-	3.0(3)	0.15(2)
		1008.6	M1+E2	5^-	18.2(16)	0.77(7)
4383.3 [a]	6^-	1185.6	M1+E2	5^-	2.6(5)	0.25(7)
4423.6	6^+	386.3 [b]	E1	7^-		0.08(3)
		462.2 [b]	E1	5^-		0.09(4)
		715.2	E1	5^-		0.10(3)
		1225.9	E1	5^-	36.9(18)	1.10(5)
4610.7	8^+	187.1 [b]	E2	6^+		0.77(7)
		227.6 [b]	M2	6^-		0.08(3)
		404.4 [b]	M2	6^-		0.51(5)
		573.4	E1	7^-		1.53(15)
		690.7 [b]	M2	6^-		0.32(12)

		902.3 [b]	E3	5^-		0.20(5)
		1413.0	E3	5^-	100.0	80,5(25)
4680.3 [a]	7^-	760.3	M1+E2	6^-	5.8(6)	
4860.8	8^+	250.0	M1+E2	8^+	9.6(5)	12.1(4)
		823.3	E1	7^-	2.5(5)	3.58(16)
		1663.0 [d]	E3	5^-		< 0.1
4895.2	10^+	34.4 [e]	E2	8^+		15.7 tot [e]
		284.5	E2	8^+		55.5(6)
		857.7	E3	7^-		12.5(4)
5010.6	9^+	149.8 [b]	M1	8^+	0.70(15)	
		399.9	M1	8^+	9.8(3)	
5162.1 [a]	9^+	151.5	M1	9^+	0.8(2)	
		551.5	M1	8^+	1.4(2)	
5326.4	9^+	465.6 [b]	M1	8^+	2.9(4)	
		715.7 [b]	M1	8^+	2.1(3)	

TAB.2

E_{level} [keV]	I^{π}	E_{gamma} [keV]	I^{π} final	multipolarity	Intensity in beam	Intensity off beam
4895.2	10^+	see Table I				
5069.2	10^+	174.0(1)	10^+	M1	11.2(4)	
5235.4	11^+	340.2(1)	10^+	M1+E2	100.0	100*
5749.6	11^+	514.2(3)	11^+	(M1)	0.5(2)	
		680.4(1)	10^+	M1+E2	18.2(6)	17(3)
		854.5(1)	10^+	(M1)	2.9(2)	
6100.7	12^+	351.2(1)	11^+	M1+E2	11.0(4)	12(2)
		865.3(1)	11^+	M1+E2	56.1(15)	65(3)
		1205.5(1)	10^+	(E2)	3.8(2)	
6435.0	12^-	685.5(3)	11^+	(E1)	0.6(2)	
		1199.5(1)	11^+	(E1)	5.8(4)	
6448.5	13^-	347.8(1)	12^+	E1	49.4(15)	63(6)
		698.9(2)	11^+	(M2)	1.0(2)	
		1213.4(3)	11^+	(M2)	1.3(3)	
		1379.4(1)	10^+	(E3)	4.1(3)	
		1553.2(1)	10^+	E3	8.4(2)	12(3)
6743.5	14^-	295.0	13^-	M1+E2	30.4(12)	58(2)
		642.7(2)	12^+	(M2)	1.5(2)	
		993.9 [a]	11^+	(E3)	<0.3	
		1508.0(1)	11^+	E3	38.9(14)	69(3)
7528.8	13^-	1080.2(2)	13^-	(M1)	1.1(2)	
		1428.1(2)	12^+	(E1)	4.0(3)	4(1)
		2634(2)	10^+	(E3)	0.2(2)	
7974.1	14^-	445.2(1)	13^-	(M1)	2.6(3)	
		1230.6(1)	14^-	M1+E2	12.8(4)	19(3)
8027.1	15^-	53.0(1)	14^-	(M1)	11.6(8) [b]	
		498.4(1)	13^-	(E2)	1.8(3)	
		1283.6(1)	14^-	M1+E2	10.0(3)	21(3)
		1578.5(1)	13^-	E2	7.4(3)	12(2)
8150.6(4)	(15^-)	123.2(4)	15^-	(M1)	1.0(6)	

8264.5	15^-	237.4(1)	15^-	(M1)	3.0(3)	4(1)
8350.8	15^-	323.7(2)	15^-	(M1)	9.2(5)	12(2)
		376.8(2)	14^-	(M1)	1.8(3)	3(1)
		1607.4(3)	14^-	(M1)	5.1(7)	4(1)
		1902.0(6)	13^-	(E2)	1.3(5)	2(1)
8600.7	16^-	249.9(1)	15^-	M1	4.8(6)	7(1)
		450.1(3)	(15^-)	(M1)	1.9(5)	
		573.5(2)	15^-	(M1)	1.7(3)	
8723.5	16^-	459.0(1)	15^-	(M1)	2.6(3)	8(2)
		1979.9(2)	14^-	(E2)	2.3(4)	7(1)
8812.8	17^-	89.3[b)]	16^-	(M1)	5.3(5) [b)]	14(3) [b)]
		212.1(1)	16^-	M1+E2	5.4(3)	15(2)
		785.6(1)	15^-	E2	6.1(3)	16(2)
9061.3	17^+	2317.8(1)	14^-	E3	28.7(8)	100(6)
9103.0(2)	18^+	41.7 [b)]	17^+	(M1)	24.7(8) [b)]	
		290.2(2)	17^-	E1	11.6(8)	47(5)
9394.3	19^+	291.3(1)	18^+	M1+E2	12.7(7)	102(5)
10135.8	$(18^-,19^+)$	1032.8(1)	18^+	(E1 or M1)	1.4(2)	10(1)
10136.2	19^+	741.9(1)	19^+	(M1)	2.0(2)	
10195.9(2)	20^+	801.6(2)	19^+	M1	5.9(5)	16(2)
10341.9	20^-	145.8(2)	20^+	E1		7(1)
		206.1(2)	$(18^+,19^+)$	(E2 or E1)		7(1)
		947.6(1)	19^+	E1	6.4(3) [c)]	126(5)
10357.3	(20^+)	963.0(1)	19^+	(M1)	4.1(4)	3(2)
10371.0	20^+	175.0(2)	20^+	(M1)	0.7(1)	
		234.8(2)	19^+	(M1)	1.2(2)	
10531.3(2)	(20^+)	160.1(4)	20^+	(M1)	0.5(2)	
		395.1(2)	19^+	(M1)	0.6(2)	
10552.4(2)	(20^+)	356.5(2)	20^+	(M1)	0.7(2)	

10934.3	21^-	592.4(1)	20^-	(M1)	1.9(3)	
11360.9	23^+	1019.0(1)	20^-	E3	5.1(3) [c]	105(5)
11958.2(2)	24^+	597.3(2)	23^+	(M1)	2.3(3)	32(3)
12949.3	25^+	991.2(1)	24^+	M1	0.9(3)	33(3)
		1588.4(1)	23^+	E2	1.1(3)	68(4)
13536.0	26^-	586.7(1)	25^+	(E1)	0.5(2)	18(2)
13674.7	28^-	138.7(2)	26^-	E2		8(1)
		725.4(1)	25^+	E3	1.9(3) [c]	72(4)

TAB. 3

E_{gamma}	I_{gamma} Pb+Pb	I_{gamma} Ca+Pb
189.2(1)	77(4)	70(7)
220.9(3)	20(3)	18(4)
244.3(2)	17(2)	18(4)
341.3(2)	100*	100*
578.0(2)	72(4)	74(7)
676.5(2)	52(4)	61(7)
723.4(3)	57(6)	57(8)
861.5(4)	44(5)	52(8)
906.9(4)	22(5)	37(7)
1077.0(5)	27(7)	17(5)
1208.3(3)	94(9)	63(8)

TAB. 4

E_{gamma}	α_{tot}	multipolarity	α_{tot} theoretical
138.7	1.3(4)	E2	1.65
145.8	0.8(6)	(E1)	0.17
174.0	1.8(2)	M1	1.94
187.1	0.7(2)	E2	0.54
206.1	0.3(2)	(E2, E1)	0.39
212.1	1.2(3)	M1	1.1
227.6	4(2)	M2	4.0
290.2	< 0.25	E1	0.032
291.3	0.41(8)	M1+E2	0.45
295.0	0.40(6)	M1+E2	0.38
340.2	0.31(4)	M1+E2	0.30
347.8	0.06(4)	E1	0.021
351.2	0.31(6)	M1+E2	0.28
404.4	0.70(14)	M2	0.61

TAB. 5

E_{gamma}	E_i	I^{π} init	I^{π} final	A_2	A_4	multipolarity	δ
174.0	5069.2	10^+	10^+	0.36(4)	- 0.06(7)	M1	
212.1	8812.8	17^-	16^-	-0.03(5)		M1+E2	+0.11(4)
249.9	8600.7	16^-	15^-	-0.18(9)		M1	
284.5[a)]	4895.2	10^+	8^+	0.25(7)		E2	
290.2	9103.0	18^+	17^-	-0.19(12)		E1	
291.3	9394.3	19^+	18^+	0.03(2)		M1+E2	+0.16(2)
295.0	6743.5	14^-	13^-	-0.68(2)	0.03(2)	M1+E2	-0.50(4)
340.2	5235.4	11^+	10^+	0.03(3)	0.04(5)	M1+E2	+0.17(3)
347.8	6448.5	13^-	12^+	-0.18(5)	-0.03(7)	E1	
351.2	6100.7	12^+	11^+	-0.08(3)		M1+E2	+0.08(3)
399.9	5010.6	9^+	8^+	-0.17(4)	-0.07(6)	M1	
680.4	5749.6	11^+	10^+	-0.26(6)		M1+E2	-0.06(5)
725.4	13674.7	28^-	25^+	0.31(10)	0.07(12)	E3	
785.6	8812.8	17^-	15^-	0.29(3)	-0.08(3)	E2	
801.6	10195.9	20^+	19^+	-0.29(11)	0.13(13)	M1	
865.3	6100.7	12^+	11^+	0.00(2)	0.00(2)	M1+E2	+0.14(2)
947.6	10342.9	20^-	19^+	-0.15(2)	0.02(2)	E1	
991.2	12949.3	25^+	24^+	-0.28(9)		M1	
1019.0	11360.9	23^+	20^-	0.47(3)		E3	
1230.6	7974.1	14^-	14^-	0.23(3)	0.09(5)	M1+E2	-0.32(9) or +0.65(15)
1283.6	8027.1	15^-	14^-	-0.73(4)	0.00(4)	M1+E2	$-0.61(^{+9}_{-16})$
1413.0[a)]	4610.7	8^+	5^-	0.34(1)	-0.03(2)	E3	

1428.1	7528.8	13^-	12^+	-0.21(18)		(E1)
1508.0	6743.5	14^-	11^+	0.41(1)	0.00(3)	E3
1553.2	6448.5	13^-	10^+	0.57(13)		E3
1578.5	8027.1	15^-	13^-	0.24(4)		E2
1588.4	12949.3	25^+	23^+	0.22(9)		E2
2317.8	9061.3	17^+	14^-	0.42(3)	-0.03(5)	E3
2614.5[a)]	2614.5	3^-	0^+	0.34(2)	-0.04(3)	E3

TAB. 6

E_{level}[keV]	I^{π}	$T_{1/2}$[ns]	E_{gamma}	mult.	Branching (%)	B(EL,ML) W.u.
4610.7	8^+	3.2(5) [a]	187.1	E2	0.90	0.095(13)
			227.6	M2	0.09	0.42(13)
			404.4	M2	0.60	0.15(2)
			573.4	E1	1.79	$5,7(9) \times 10^{-9}$
			690.7	M2	0.37	0.007(2)
			902.3	E3	0.23	0.71(17)
			1413.0	E3	94.6	12.3(20)
4895.2	10^+	535(35) [b]	34.4	E2	0.017	0.052(4)
			284.5	E2	60.7	0.0047(3)
			857.7	E3	13.7	0.355(25)
10341.9	20^-	22(3)	145.8	E1	4.9	$1.38(21) \times 10^{-7}$
			206.1	E2	4.9	0.046(10)
			„	E1	„	$5.0(11) \times 10^{-8}$
			947.6	E1	87.5	$9.1(13) \times 10^{-9}$
11360.9	23^+	12.7(15)	1019.0	E3	98.5	32.1(39)
13674.7	28^-	60(6)	138.7	E2	8.4	0.21(4)
			725.4	E3	75.2	56(7)
6448.5	13^-	0.188 [c]	1553.2	E3	12.9	15.0 [c]
			347.8	E1	75.8	1.8×10^{-5}
			698.9	M2	1.5	0.44
			1213.4	M2	2.0	0.036
			1379.4	E3	6.3	16.9
6743.5	14^-	0.42 [c]	1508.0	E3	47.2	30.0 [c]
			295.0	M1	29.5 [d]	6.05×10^{-4}
			295.0	E2	7.4 [d]	0.61
			642.7	M2	1.8	0.35
			993.9	E3	< 0.36	< 4
^{209}Pb [e]	$15/2^-$	1.36(30)	1422.6	E3	90.0	26(7)
			643.5	M2	9.9	0.57(14)
^{208}Pb [e]	3^-	0.0167(3)	2614.5	E3	100.0	33.8(6)

Figure Captions – 208Pb

1. Coincidence spectra showing four new transitions depopulating the 4611-keV, 8^+ level in ^{208}Pb. Off-beam DDD data from the ^{208}Pb + ^{208}Pb experiment were used with double coincidence gates placed as indicated in the corresponding panels. The 404-keV *M*2 (a), 187-keV *E*2 (b), 228-keV *M*2 (c), and 902-keV *E*3 (d) transitions represent decay branches from the 8^+ level with respective intensities of 0.51, 0.77, 0.08, and 0.20% of the 2615-keV transition (see Table I).
2. (Color online) Partial level scheme for ^{208}Pb limited to states with $I \leq 10$ observed in the ^{208}Pb + ^{208}Pb measurement. For each transition, the arrow width reflects the prompt population intensity. Transitions new to this work are marked in red.
3. Low- (a,b) and high- (c,d) energy parts of spectra presenting transitions that precede in time the 10^+ isomer decay in ^{208}Pb. The double gates were placed on delayed γ rays below the isomer and the spectra display prompt (a,c) and delayed (b,d) transitions located above the 10^+ isomer (see text). The ^{208}Pb + ^{208}Pb coincidence data were used and ^{208}Pb transitions are indicated by energies. Those associated with complementary Pb isotopes are marked with symbols explained in the legend.
4. The ^{208}Pb level scheme including all the states located above the 10^+ isomer established in the present work. The widths of the arrows reflect intensities involved in both prompt and off-beam population. See text for details on the construction of the level scheme and on spin-parity assignments.
5. Examples of coincidence spectra addressing two specific parts of the level scheme of Fig. 4. The coincidence gates were placed in the prompt PP matrix from the ^{208}Pb + ^{208}Pb data, but with a preselection requiring a coincidence with delayed transitions from the 10^+ isomer decay. The spectrum obtained with a gate placed on the 680-keV transition (a) enhances the relatively weak decay branch below the 14^-_1 yrast level and includes also the weak 686- and 699-keV lines (see text). The spectrum in panel (b) was obtained by summing spectra with gates placed on the 1231-, 1284-, and 1579-keV transitions that collect most of the intensity in the depopulation of the 14^-_2 and 15^-_1 levels. A strong enhancement is observed of transitions from the yrast decay branches that populate negative-parity states and compete with the most intense 2318-keV γ ray (see text). In both panels, the ^{208}Pb transitions are marked by their respective energy, while those associated with complementary Pb isotopes are identified by the symbols indicated in the legend.
6. Coincidence spectra with gates placed on the unresolved doublet of 290- and 291-keV γ rays in (PP) prompt (a) and (dd) delayed matrices preselected by requiring a coincidence with delayed (D) transitions below the 10^+ isomer. The energy range selected here enables a comparison between prompt and delayed intensities for the main transitions observed in the high-spin yrast decay which involves three isomers. The inserts provide the highest-energy parts of the data with the most intense 2318-keV line. The ^{208}Pb transitions are indicated by their respective energy and those from complementary Pb isotopes are marked according to the legend (see text).
7. Off-beam coincidence spectra obtained from the ddD cube by placing D gates on transitions below the 10^+ isomer and delayed gates on intense transitions in the highest-spin part of the level scheme (see text). Spectra with d gates selecting the 1019- (a), 1588- (b), and 725-keV(c) lines are displayed within the energy range crucial for the section of the level scheme involving three upper isomers. The ^{208}Pb transitions are indicated by their respective energy and open triangles mark those associated with the ^{202}Pb complementary fragments. The latter ones represent true

coincidence events, as the yield of complementary Pb isotopes can be seen to be shifted to lower masses. Note also that the isomeric half-life in ^{202}Pb falls into the range defined by the d delayed time gate.

8. Off-beam coincidence spectra supporting the placement of low-energy transitions in isomeric decays. With the same selection of gates in the ddD cube as in Fig. 7, the data gated on the 587-keV line (a) displays the 139-keV decay branch from the 28^- isomer while spectra with gates placed on the 802- (b) and 1033-keV (c) γ rays, respectively, display the 146- and 206-keV transitions depopulating the 20^- isomer (see Fig. 4).
9. Time distributions used to determine the half-lives of the three new isomeric states in ^{208}Pb (a) and to achieve a new determination of the 10^+ isomer half-life (b). These spectra were obtained by placing gates on the most intense transitions above (G1) and delayed γ rays below (G2) the isomers, as indicated in the various panels. The G1 transitions used in the $T_{1/2}$ determination for the 60-ns, 28^- isomer (bottom of panel (a)) include the seven most intense lines displayed in the spectrum of Fig. 10 (see text for details).
10. Spectra of ^{208}Pb prompt (P) transitions located above the 28^-, highest-spin isomer extracted from the ^{208}Pb + ^{208}Pb (a) and ^{48}Ca + ^{208}Pb (b) coincidence data. The PDD coincidence cubes were used with double-delayed D gates placed on all combinations of the most intense γ rays between the 28^- and 10^+ isomers (see Fig. 4). The ^{208}Pb transitions are indicated by their energies and those from the complementary Pb (a) and Ca (b) isotopes are marked by symbols provided in the legends. The presence of γ rays in both the higher-statistics (a) and the cleaner (b) spectra served as a criterion to identify the transitions listed in Table III.
11. Examples of angular distribution results obtained from the ^{208}Pb + ^{208}Pb measurement. Experimental points were fitted with A_2 and A_4 terms and, exceptionally, with an A_2 term only (see text and numerical results listed in Table V). These distributions were selected to show characteristic cases; *e.g.*, *E*3 transitions (2318, 1508, 1019, and 725 keV) exhibiting large, positive A_2 coefficients, mixed *M*1/*E*2 ΔI=1 transitions (295, 1284 keV) with large negative A_2 values, and nearly isotropic mixed *M*1/*E*2 transitions (291, 865 keV).
12. Comparison between experimental and calculated 1p-1h yrast and near-yrast states in ^{208}Pb. The full shell-model calculations performed within two approaches are described in the text and the calculated levels are shown on either side of the experimental levels. To simplify the comparison, the positive- and negative-parity levels are displaced relative to one another and the experimental yrast levels are connected by dashed lines to their proposed theoretical counterparts.
13. Comparison between experimental and calculated states in ^{208}Pb above the 10^+ isomer. The format is the same as in Fig.12. The description of the full shell-model calculations involving, in this case, 2p-2h excitations as well as the detailed discussion of the comparison between the theoretical and experimental levels can be found in the text. Using a truncated configuration space, the approach labelled (2016) also included a computation of 3p-3h excitations, and the corresponding results are displayed on the right with this specific group of levels framed in a separate box.
14. (Color online) Energies of high-spin levels in ^{208}Pb plotted versus the $I(I+1)$ product to test the "rotational" interpretation of the observed yrast and near-yrast states. All of the observed levels are included with the parity indicated by blue diamonds (negative) and red circles (positive). The result of the straight line fit for points from $I = 6$ to $I = 28$, with a fixed, 5.0 MeV, energy gap is displayed in the figure as well. The "rotation"

and the resulting moment of inertia interpretation are discussed in the text. The four highest-spin points placed in brackets correspond to unassigned levels identified above the 28^- isomer. They are displayed here under the conservative assumption that the decay γ rays are all of $M1$ character (see text).

Fig. 1

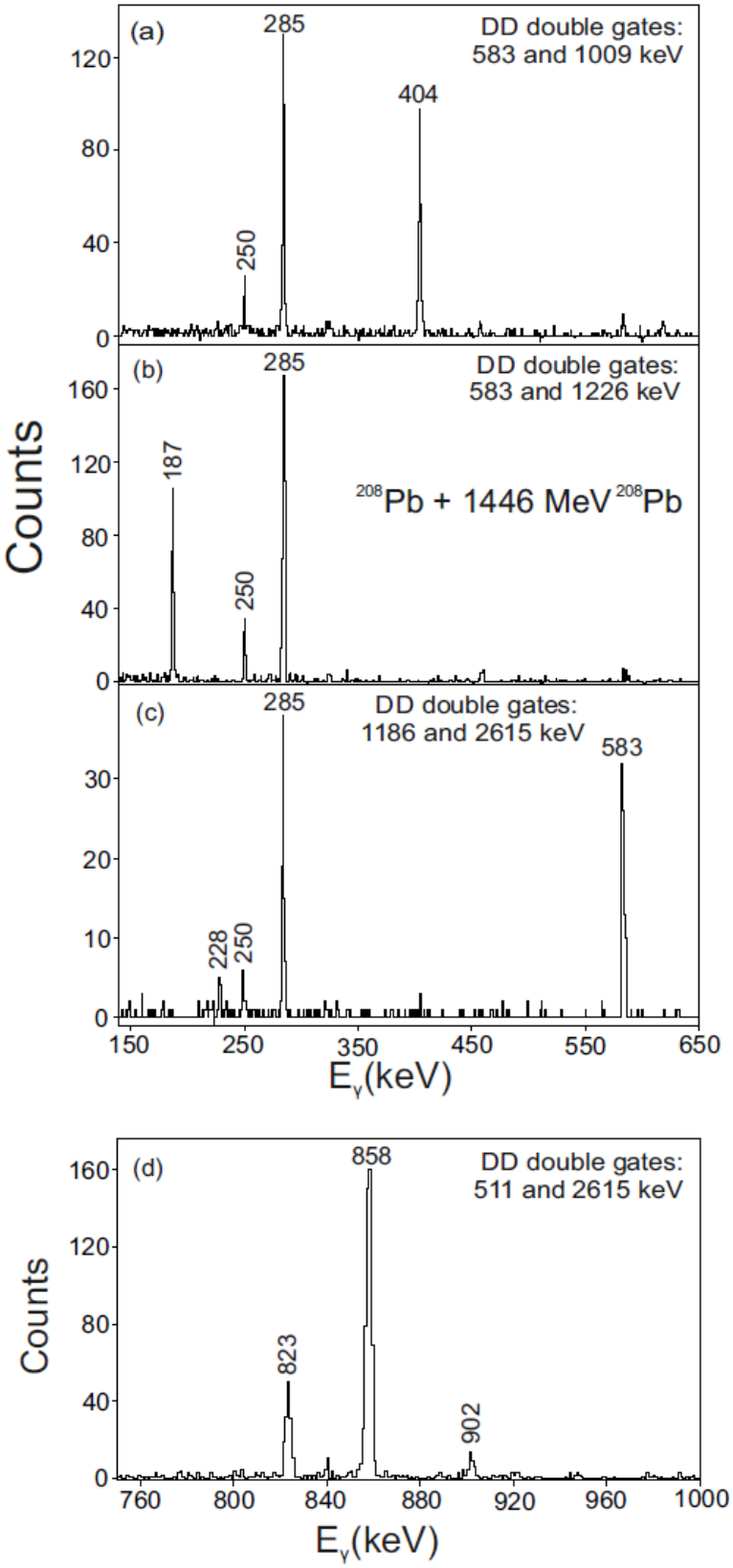
(a)
285
404
250
DD double gates:
583 and 1009 keV
(b)
285
187
250
DD double gates:
583 and 1226 keV
^{208}Pb + 1446 MeV ^{208}Pb
(c)
285
583
228
250
DD double gates:
1186 and 2615 keV
Counts
E_γ(keV)
(d)
858
823
902
DD double gates:
511 and 2615 keV
Counts
E_γ(keV)

Fig. 2

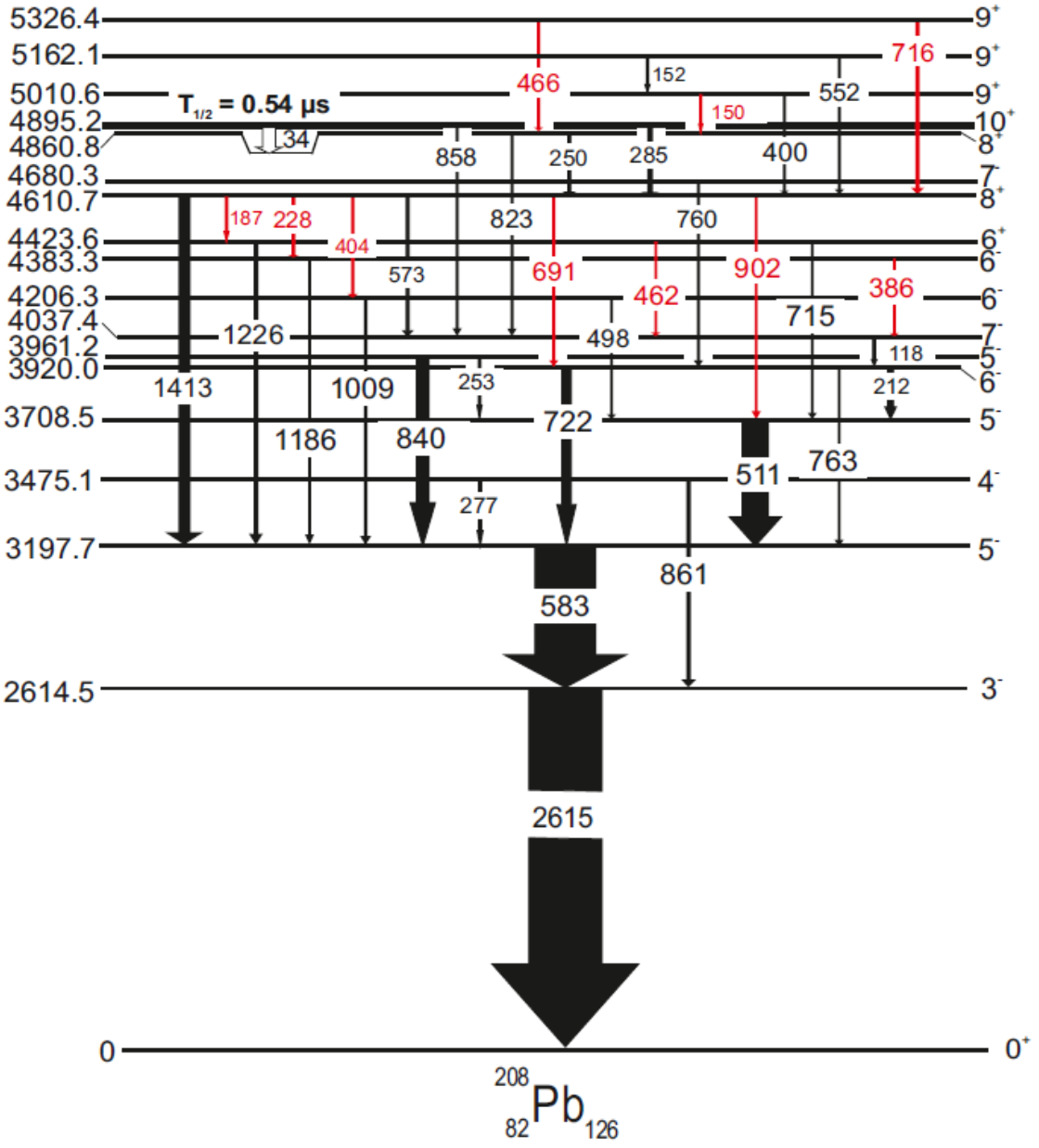
5326.4
5162.1
5010.6
4895.2
4860.8
4680.3
4610.7
4423.6
4383.3
4206.3
4037.4
3961.2
3920.0
3708.5
3475.1
3197.7
2614.5
0
$T_{1/2}$ = 0.54 μs
34
466
152
552
716
150
858
250
285
400
187
228
404
823
760
573
691
462
902
386
715
1226
498
118
1413
1009
253
212
722
1186
840
763
511
277
861
583
2615
$^{208}_{82}Pb_{126}$

Fig. 3

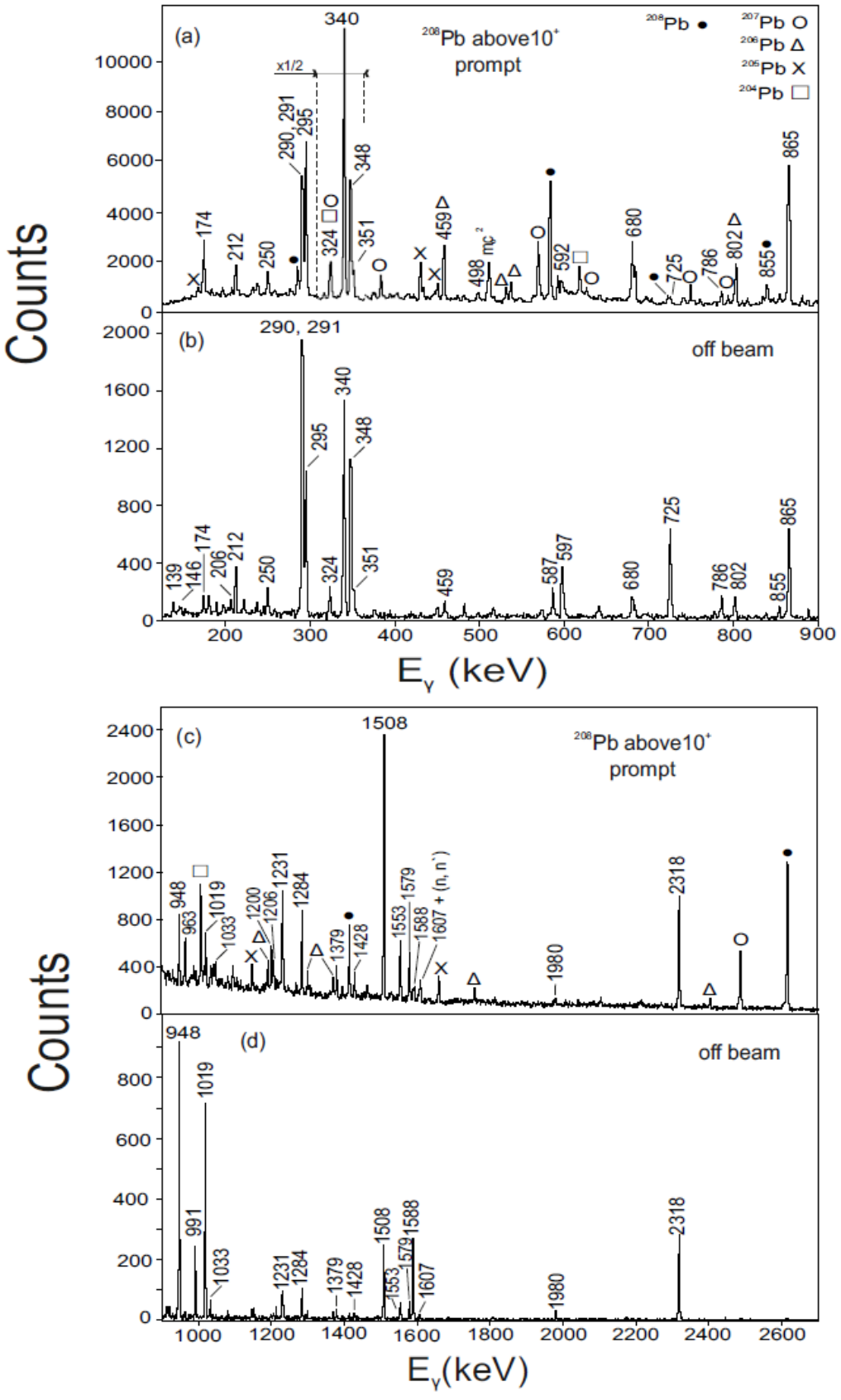
Counts
(a)
^{208}Pb above10^{+}
prompt
^{208}Pb ●
^{207}Pb O
^{206}Pb Δ
^{205}Pb X
^{204}Pb □
x1/2
340
290, 291
295
348
865
174
212
250
324
351
459
498
mc^2
592
680
725
786
802
855
(b)
off beam
290, 291
340
295
348
865
174
139
146
206
212
250
324
351
459
587
597
680
725
786
802
855
E$_\gamma$ (keV)
Counts
(c)
^{208}Pb above10^{+}
prompt
1508
948
963
1019
1033
1200
1206
1231
1284
1379
1428
1553
1579
1588
1607 + (n, n')
1980
2318
(d)
off beam
948
1019
991
1033
1231
1284
1379
1428
1508
1553
1579
1588
1607
1980
2318
E$_\gamma$(keV)

Fig. 4

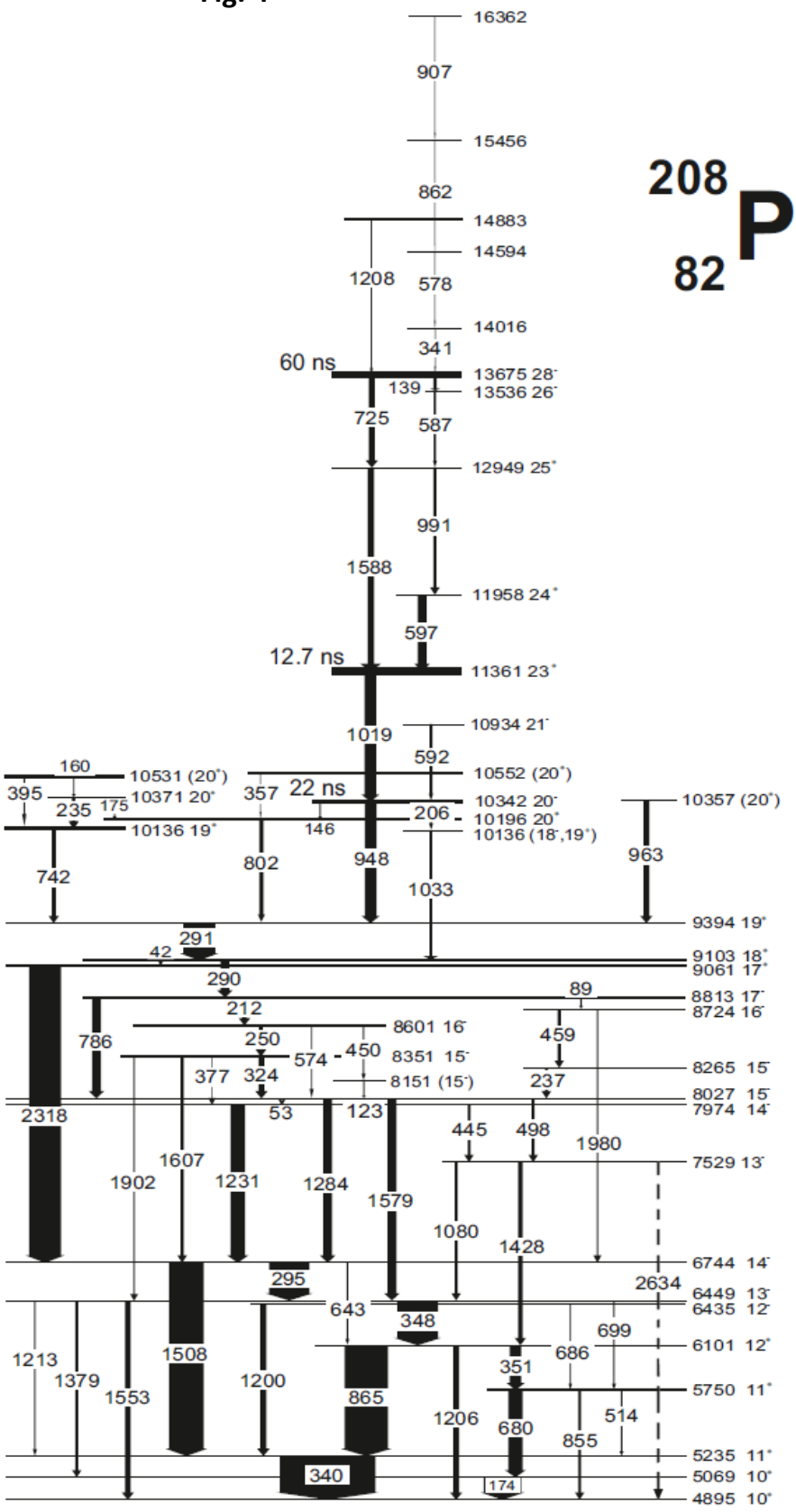
208 82 Pb 126
16362
907
15456
862
14883
14594
1208
578
14016
341
60 ns
13675 28⁻
139
13536 26⁻
725
587
12949 25⁺
991
1588
11958 24⁺
597
12.7 ns
11361 23⁺
1019
10934 21⁻
592
160
10531 (20⁺)
10552 (20⁺)
395
10371 20⁺
357
22 ns
10342 20⁻
10357 (20⁺)
235
175
206
10196 20⁺
10136 19⁺
146
10136 (18⁻,19⁺)
963
742
802
948
1033
9394 19⁺
291
42
9103 18⁺
9061 17⁺
290
89
8813 17⁻
212
8724 16⁻
8601 16⁻
786
250
459
574
450
8351 15⁻
8265 15⁻
377
324
8151 (15⁻)
237
8027 15⁻
2318
53
123
7974 14⁻
445
498
1980
1607
7529 13⁻
1902
1231
1284
1579
1080
1428
6744 14⁻
295
2634
643
6449 13⁻
348
6435 12⁻
699
1213
1508
686
6101 12⁺
1379
1200
351
5750 11⁺
1553
865
1206
680
514
855
5235 11⁺
340
5069 10⁺
174
4895 10⁺

Fig. 5

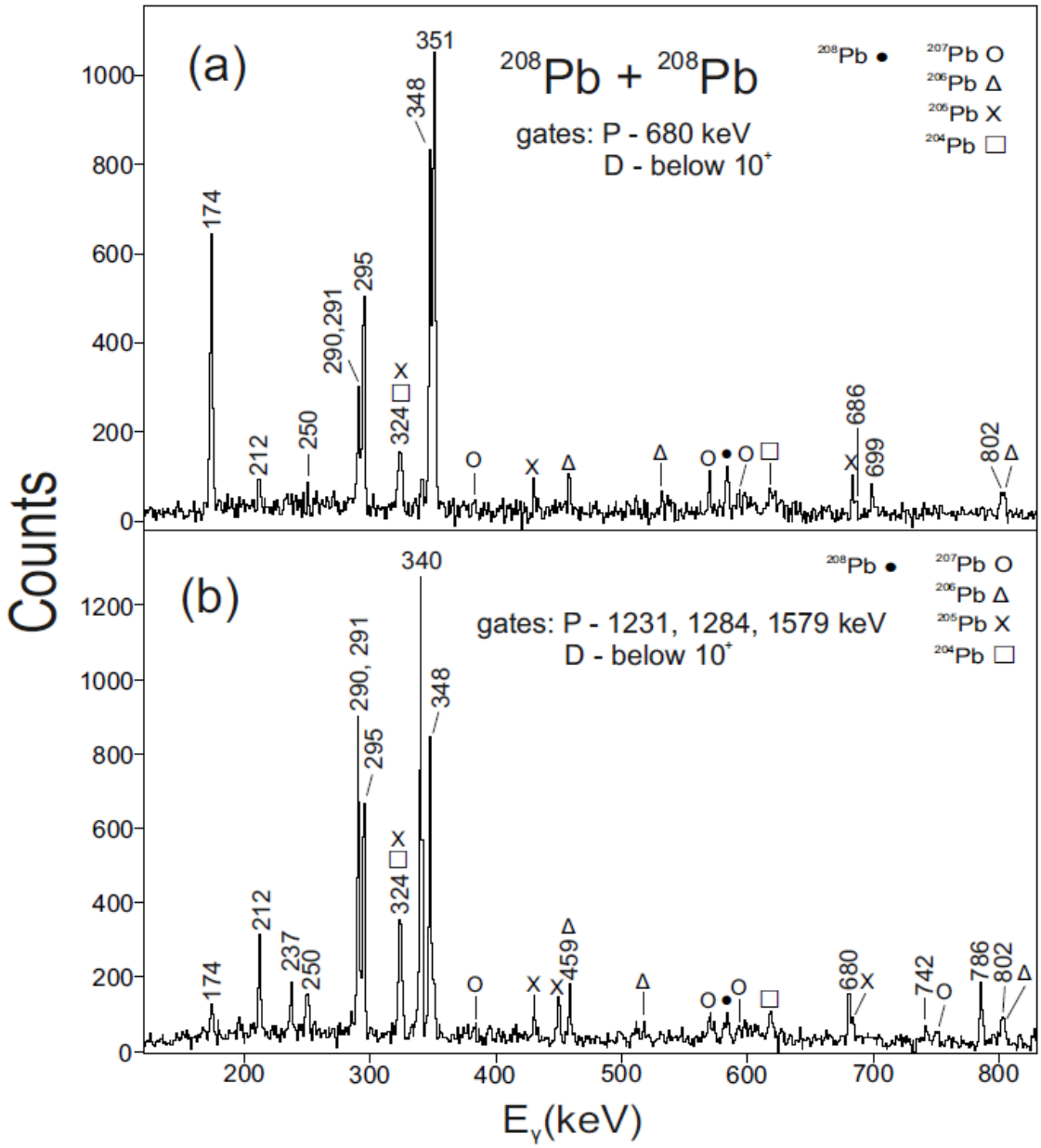
(a)
^{208}Pb + ^{208}Pb
gates: P - 680 keV
D - below 10^{+}
^{208}Pb ●
^{207}Pb O
^{206}Pb Δ
^{205}Pb X
^{204}Pb □
174
212
250
290,291
295
324
348
351
686
699
802
(b)
gates: P - 1231, 1284, 1579 keV
D - below 10^{+}
340
459
680
742
786
Counts
E$_\gamma$(keV)

Fig. 6

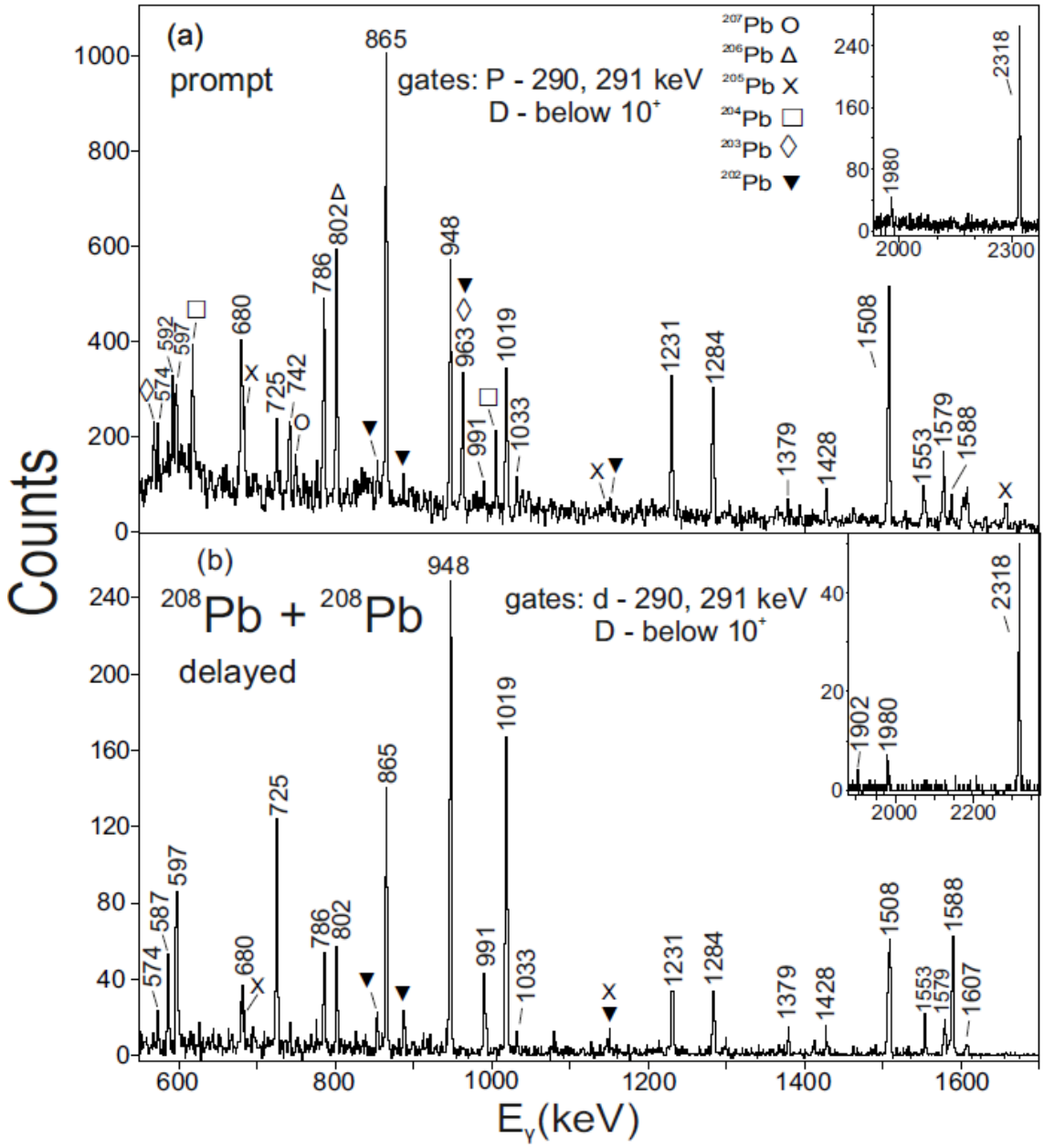
(a)
prompt
gates: P - 290, 291 keV
D - below 10+
207Pb O
206Pb Δ
205Pb X
204Pb □
203Pb ◇
202Pb ▼
865
948
802
786
680
592
597
574
725
742
963
991
1019
1033
1231
1284
1379
1428
1508
1553
1579
1588
2318
1980
(b)
208Pb + 208Pb
delayed
gates: d - 290, 291 keV
D - below 10+
948
865
725
1019
597
587
574
680
786
802
991
1033
1231
1284
1379
1428
1508
1588
1553
1579
1607
2318
1902
1980
Counts
Eγ(keV)

Fig. 7

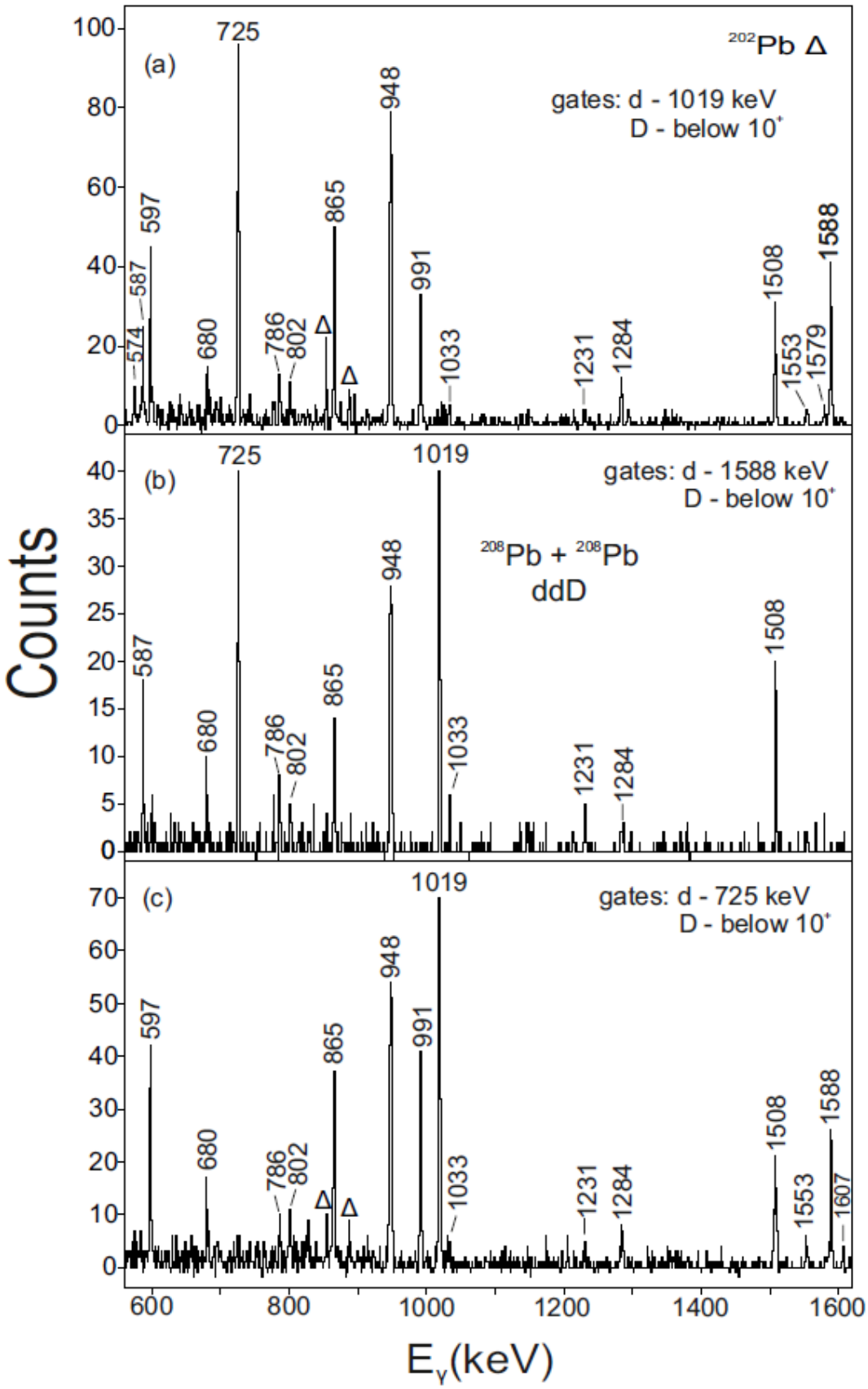
(a)
^{202}Pb Δ
gates: d - 1019 keV
D - below 10$^+$
(b)
gates: d - 1588 keV
D - below 10$^+$
^{208}Pb + ^{208}Pb
ddD
(c)
gates: d - 725 keV
D - below 10$^+$
Counts
E_γ(keV)
725
948
597
865
991
1588
1508
587
680
786
802
Δ
1033
1231
1284
1553
1579
574
1019
1607

Fig. 8

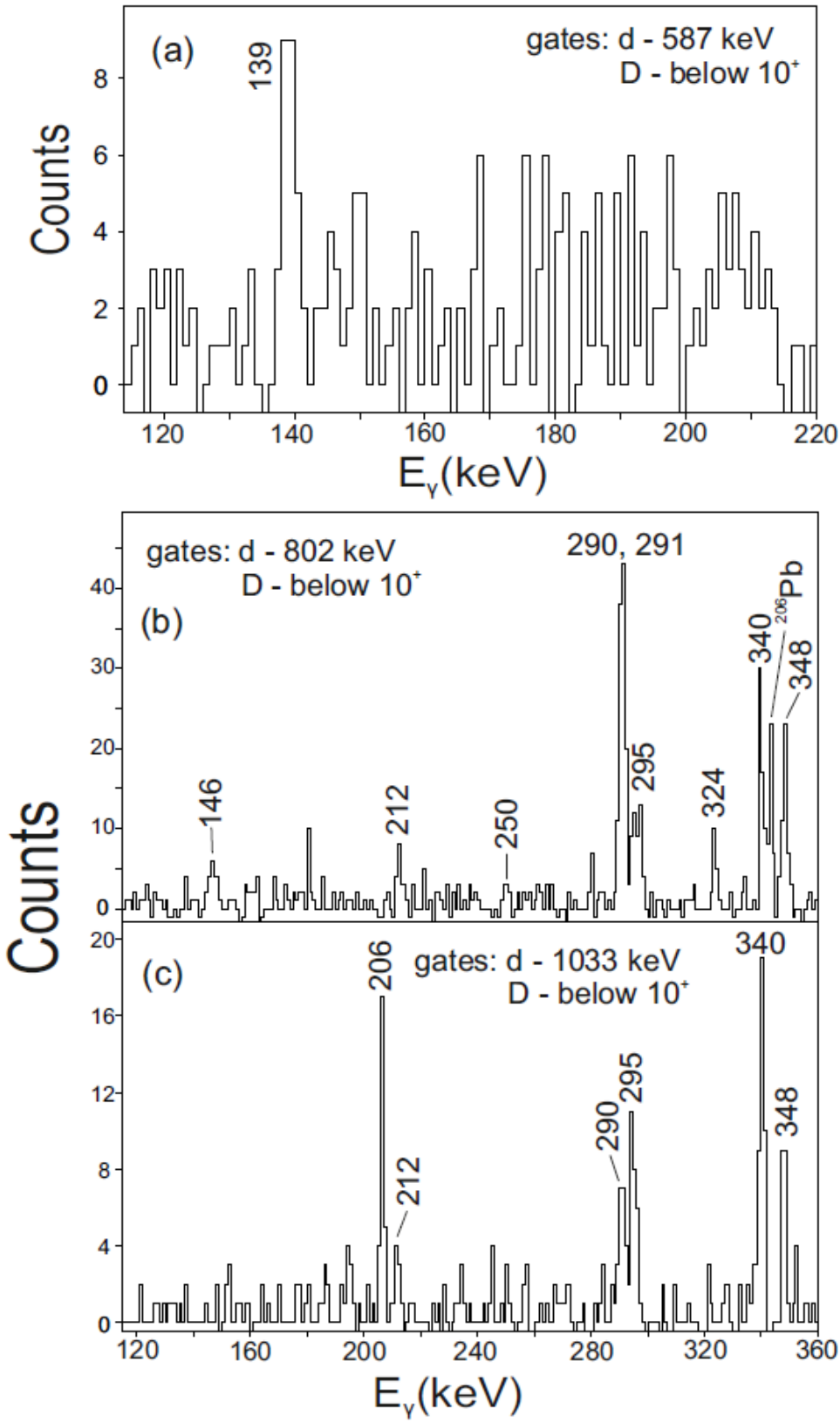
(a)
gates: d - 587 keV
D - below 10+
139
Counts
Eγ(keV)
(b)
gates: d - 802 keV
D - below 10+
290, 291
340
206Pb
348
295
324
146
212
250
(c)
gates: d - 1033 keV
D - below 10+
206
340
290
295
348
212

Fig. 9

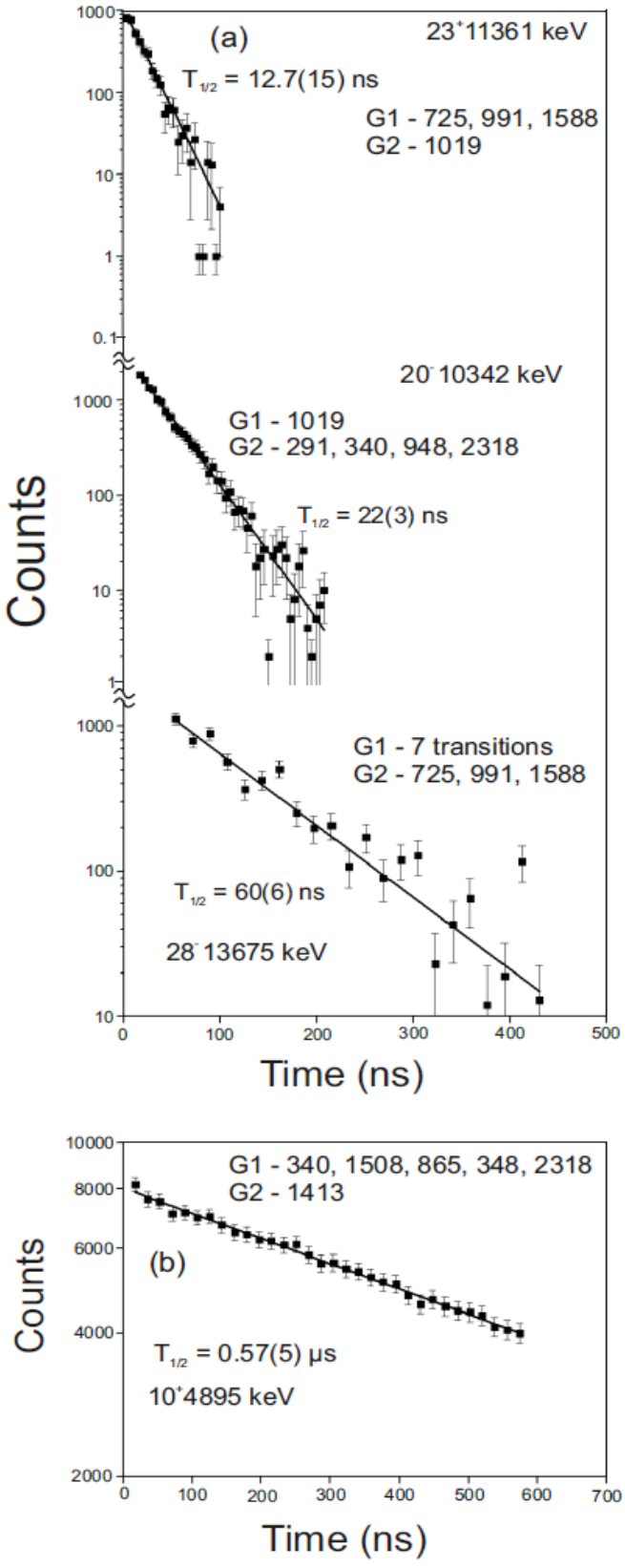
(a)
23+11361 keV
T1/2 = 12.7(15) ns
G1 - 725, 991, 1588
G2 - 1019
20- 10342 keV
G1 - 1019
G2 - 291, 340, 948, 2318
T1/2 = 22(3) ns
G1 - 7 transitions
G2 - 725, 991, 1588
T1/2 = 60(6) ns
28- 13675 keV
Counts
Time (ns)
(b)
G1 - 340, 1508, 865, 348, 2318
G2 - 1413
T1/2 = 0.57(5) μs
10+4895 keV
Counts
Time (ns)

Fig. 10

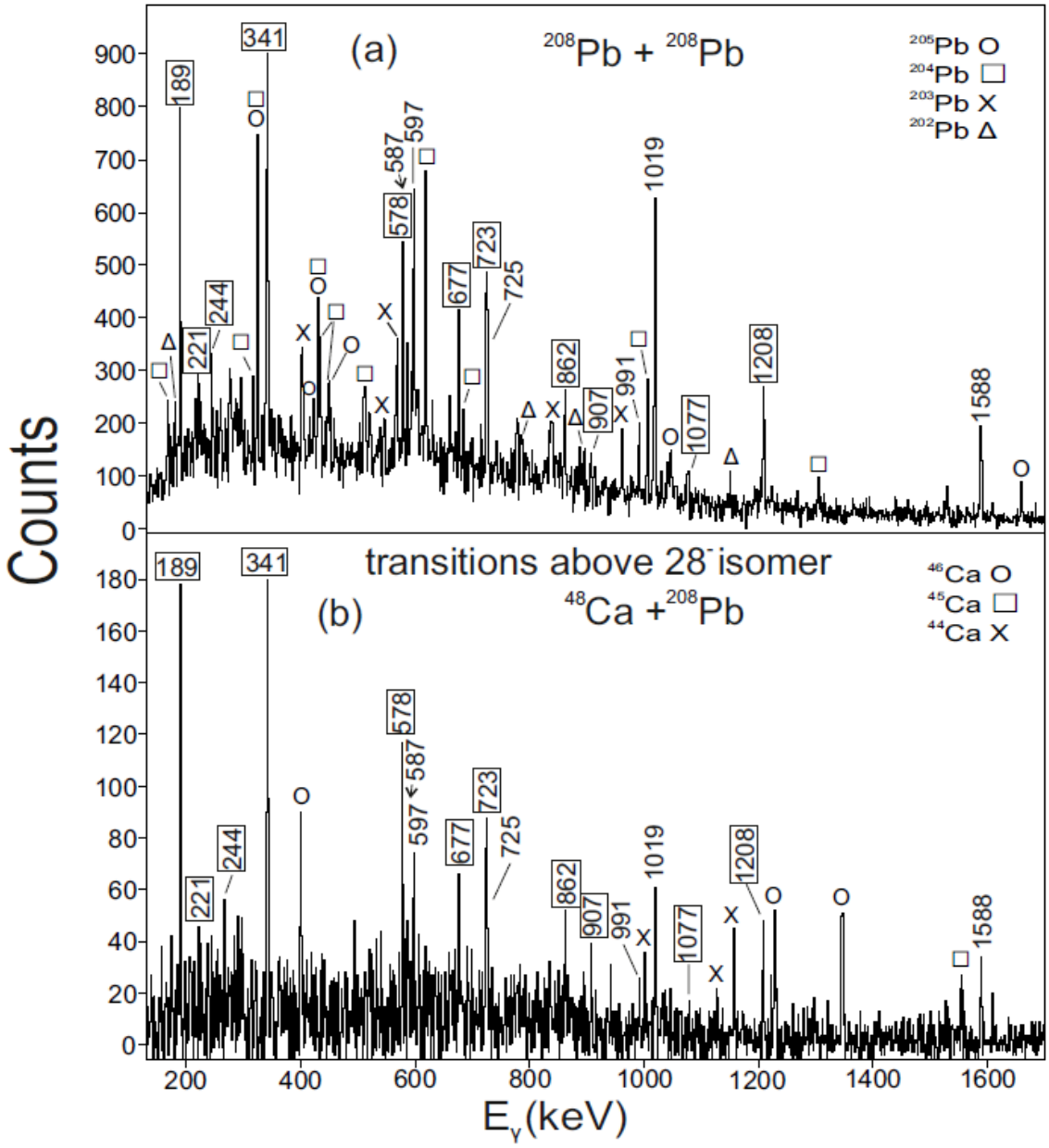
(a)
^{208}Pb + ^{208}Pb
^{205}Pb O
^{204}Pb □
^{203}Pb X
^{202}Pb Δ
189
341
221
244
578
587
597
677
723
725
862
907
991
1019
1077
1208
1588
transitions above 28⁻ isomer
(b)
^{48}Ca + ^{208}Pb
^{46}Ca O
^{45}Ca □
^{44}Ca X
Counts
E_γ(keV)

Fig. 11

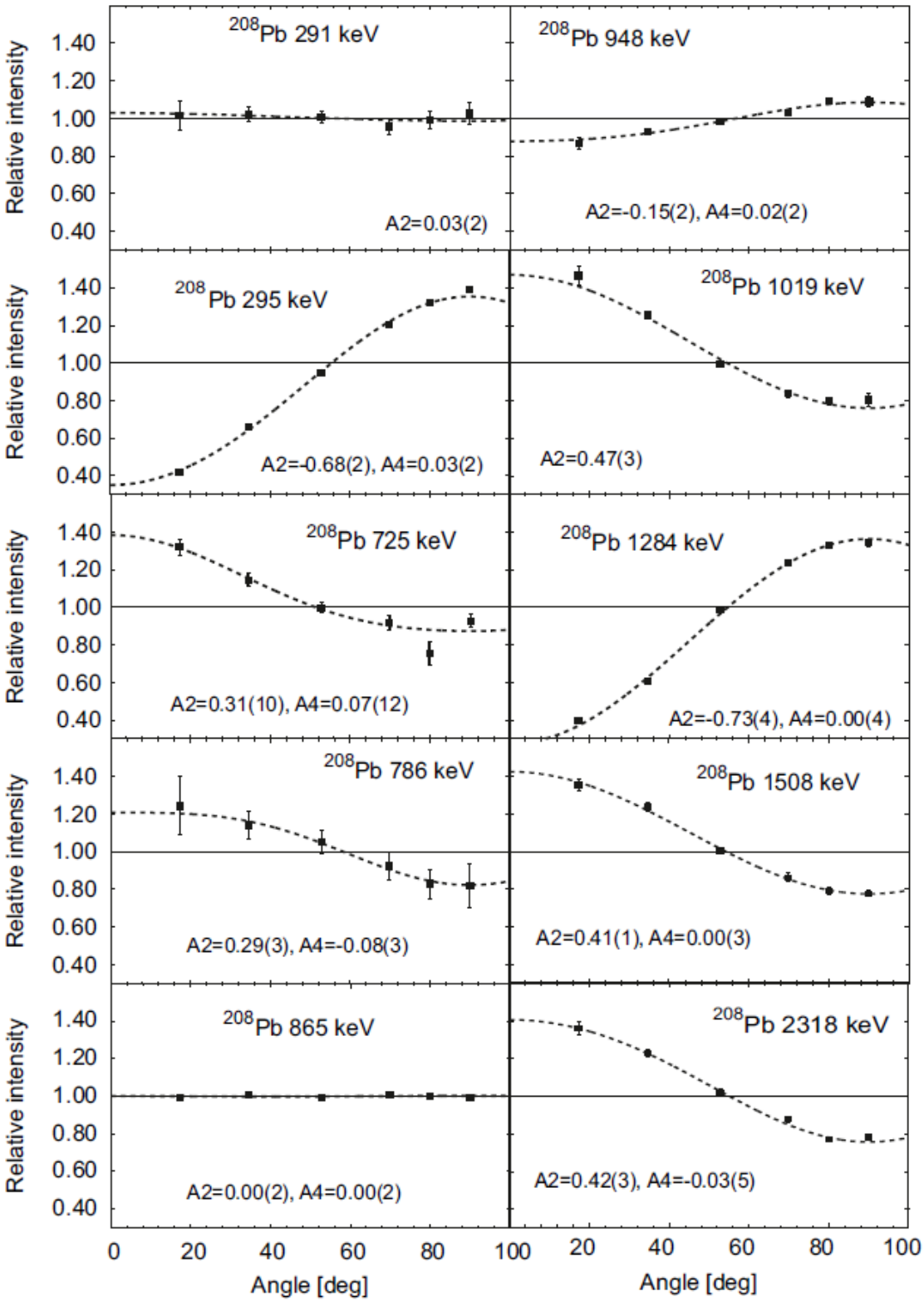
208Pb 291 keV
A2=0.03(2)
208Pb 948 keV
A2=-0.15(2), A4=0.02(2)
208Pb 295 keV
A2=-0.68(2), A4=0.03(2)
208Pb 1019 keV
A2=0.47(3)
208Pb 725 keV
A2=0.31(10), A4=0.07(12)
208Pb 1284 keV
A2=-0.73(4), A4=0.00(4)
208Pb 786 keV
A2=0.29(3), A4=-0.08(3)
208Pb 1508 keV
A2=0.41(1), A4=0.00(3)
208Pb 865 keV
A2=0.00(2), A4=0.00(2)
208Pb 2318 keV
A2=0.42(3), A4=-0.03(5)
Relative intensity
Angle [deg]

Fig. 12

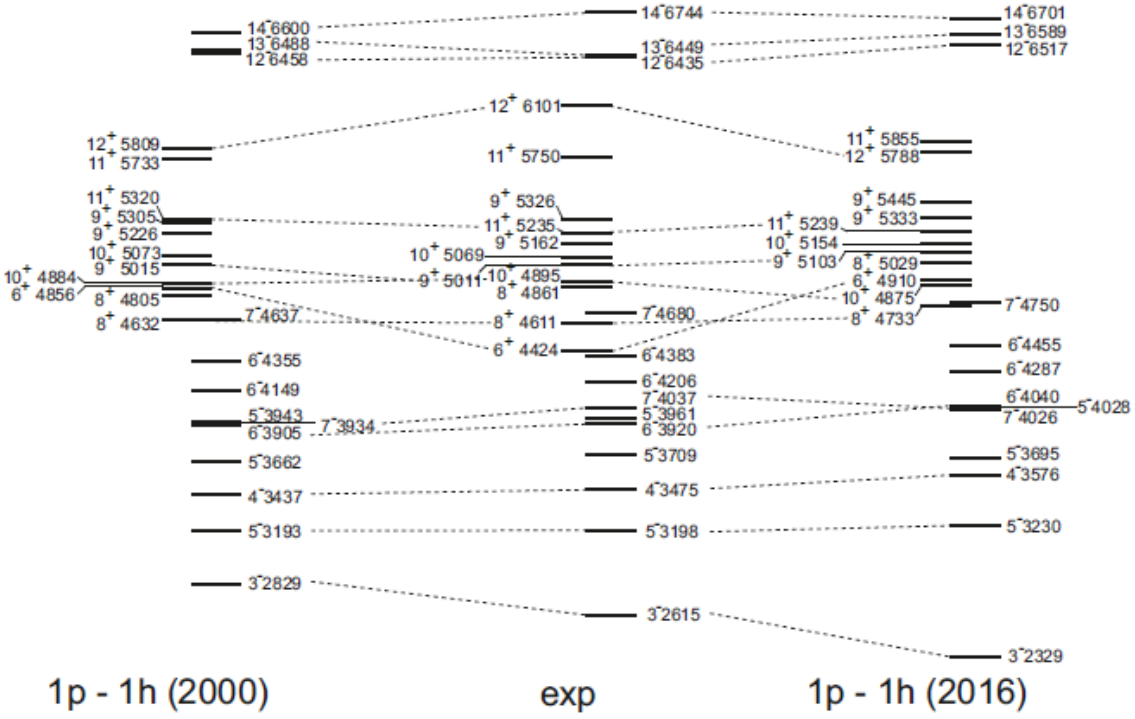
14+ 6600
13- 6488
12+ 6458
14+ 6744
13- 6449
12+ 6435
14+ 6701
13- 6589
12+ 6517
12+ 6101
12+ 5809
11- 5733
11+ 5750
11+ 5855
12+ 5788
11+ 5320
9+ 5305
9+ 5226
10+ 5073
9+ 5015
10+ 4884
6+ 4856
8+ 4805
8+ 4632
7- 4637
9+ 5326
11+ 5235
9+ 5162
10+ 5069
9+ 5011
10+ 4895
8+ 4861
8+ 4611
6+ 4424
7- 4680
9+ 5445
9+ 5333
11+ 5239
10+ 5154
9+ 5103
8+ 5029
6+ 4910
10+ 4875
8+ 4733
7- 4750
6- 4355
6- 4149
5- 3943
6- 3905
7- 3934
5- 3662
4- 3437
5- 3193
3- 2829
6- 4383
6- 4206
7- 4037
5- 3961
6- 3920
5- 3709
4- 3475
5- 3198
3- 2615
6- 4455
6- 4287
6- 4040
7- 4026
5- 4028
5- 3695
4- 3576
5- 3230
3- 2329
1p - 1h (2000)
exp
1p - 1h (2016)

Fig. 13

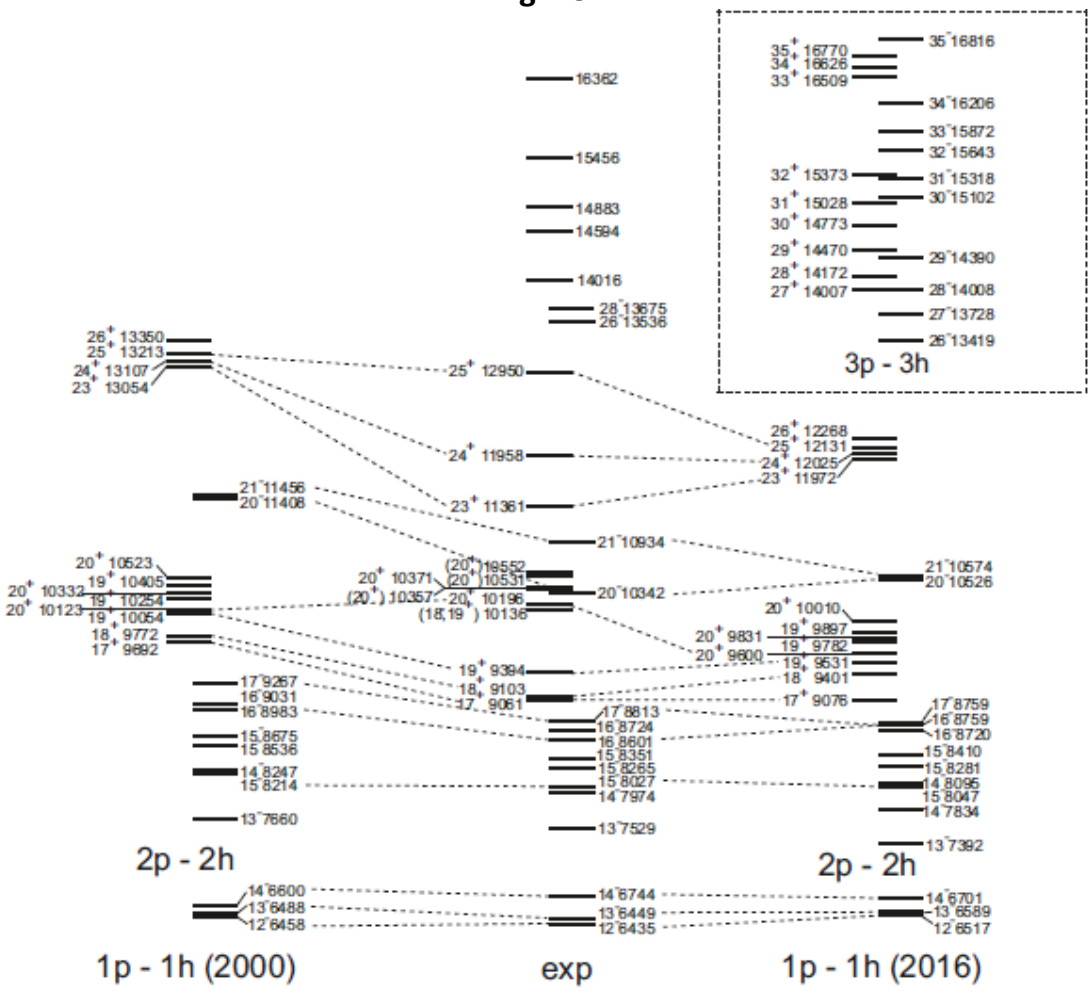

Fig. 14

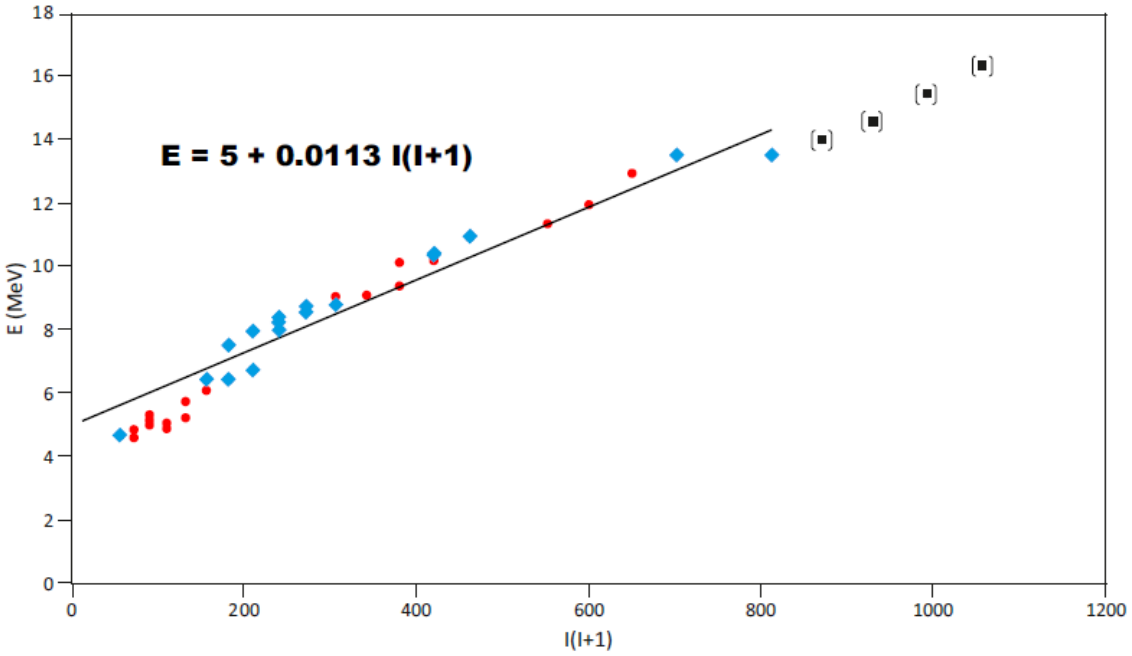
E = 5 + 0.0113 I(I+1)
E (MeV)
I(I+1)
0
2
4
6
8
10
12
14
16
18
0
200
400
600
800
1000
1200